Remote Sensing of Environment 325 (2025) 114789

Contents lists available at ScienceDirect

Remote Sensing of Environment

journal homepage: www.elsevier.com/locate/rse

Substantial increases in burned area in circumboreal forests from 1983 to 2020 captured by the AVHRR record and a new autoregressive burned area detection algorithm

Connor W. Stephens [a,*], Anthony R. Ives [b], Volker C. Radeloff [a]

[a] SILVIS Lab, Department of Forest and Wildlife Ecology, University of Wisconsin-Madison, 1630 Linden Drive, Madison, WI 53706, USA
[b] Department of Integrative Biology, 459 Birge Hall, Madison, WI 53706, USA

ARTICLE INFO

Editor: Prof Zhe Zhu

Keywords:
Wildfire
Boreal forests
Remote sensing
AVHRR
MODIS
Autoregressive time-series analysis

ABSTRACT

Wildfire maintains boreal forest health by catalyzing nutrient cycling and forest succession. However, increased annual burned area due to climate warming may facilitate forest loss and soil carbon release, which makes it important to monitor circumboreal burned area. Our goal was to characterize regional changes in circumboreal burned area from 1983 to 2020 using Advanced Very High Resolution Radiometer (AVHRR) data, and to identify the ecoregions where increases in burned area represent significant trends. We accomplished this by developing and applying a new burned area mapping algorithm that is based on an autoregressive analysis of the AVHRR and MODIS MOD09CMGv061 time series. Our algorithm worked well, and resulting burned area totals were similar to those of the MODIS MCD64A1v61 burned area product for years where both were available (2001−2020); however, the advantage of our AVHRR burned area dataset is that it extends back to 1983. Based on the resulting burned area maps, we evaluated circumboreal burned area changes and tested for significant trends. Net changes were substantial: while only 5.37 % of the circumboreal biome burned in the 1980s, 8.22 % did during the 2010s, an increase of 2.85 % (= 8.22–5.37 %) that corresponds to a proportional increase in area burned of 0.53 (= 2.85/5.37). In one ecoregion, Muskwa Slave Lake Forests, burned area more than quadrupled from the 1980s to the 2010s, and in three it more than tripled (Northern Canadian Shield Taiga, Yukon Interior Dry Forests, and Northeast Siberian Taiga). Furthermore, despite interannual variability in burned area typically being high, we found statistically significant increasing trends in burned area in seven of the twenty-three boreal ecoregions, corresponding to 19.6 % of boreal forests (35 % of North American and 11 % of Eurasian boreal forests), while only one ecoregion (Eastern Canadian Shield Taiga) had a decreasing trend. By analyzing the long-term AVHRR record, we were able to capture much larger increases in burned area than from the shorter MODIS record, allowing us to quantify how widespread and substantial these increases have been. By analyzing ecoregions, we found that north-eastern Siberian, north-western Canadian, and Alaskan boreal forests have experienced the most increases in burned area. These increases in burned area may have implications for future forest persistence and carbon storage within Eurasian and North American boreal forests.

1. Introduction

Wildfire, either of natural, accidental, or intentional origin, is a disturbance process of global significance (Krawchuk et al., 2009), affecting 500 million hectares (Mha) in 2019 alone (Lizundia-Loiola et al., 2022). Wildfires are a major source of disturbance in many ecosystems including boreal, temperate, and neotropical forests, woodlands, grasslands, and savannas (Liu et al., 2010). Wildfires can benefit wildfire-adapted forested ecosystems by facilitating succession, nutrient cycling, reducing fuel loads, and thereby minimizing the intensity and severity of subsequent wildfires (Pausas and Keeley, 2021). However, wildfire can also negatively affect plant communities when it occurs outside of its natural range of variation, threaten human health through smoke, and contribute to climate warming through greenhouse gas emissions (Bowman et al., 2020; Phillips et al., 2022).

Among global biomes, the circumboreal biome is warming and drying more rapidly than any other (Pithan and Mauritsen, 2014; IPCC, 2021), which is why the extent and frequency of wildfires is predicted to

* Corresponding author.
E-mail address: cwstephens@wisc.edu (C.W. Stephens).

https://doi.org/10.1016/j.rse.2025.114789
Received 6 August 2024; Received in revised form 15 April 2025; Accepted 25 April 2025
Available online 30 April 2025

increase there (Mhawej et al., 2015). The boreal forests of North America and Eurasia, or the circumboreal region, encompass approximately 1135 Mha, contain two-thirds of global forest (Pan et al., 2011; Bradshaw and Warkentin, 2015), and are wildfire-adapted (Bond-Lamberty et al., 2007; Talucci et al., 2022). Increases in circumboreal burned area is a major concern due to the potential for increased greenhouse gas emissions (Walker et al., 2019; Dieleman et al., 2020), permafrost degradation (Holloway et al., 2020), black carbon production (Kang et al., 2020; Ohata et al., 2021), and conversion of forests to grasslands (Whitman et al., 2019; Barrett et al., 2020). As such, we focused on the long-term changes and trends in circumboreal burned area and their variation among ecoregions within the circumboreal region.

Satellite observations can systematically map wildfires across the circumboreal region (Petropoulos et al., 2010; Giglio et al., 2015; Giglio et al., 2018), which is important because in situ mapping is infeasible due to the large number of fires in remote areas (Soja et al., 2006; Garcia-Lazaro et al., 2018). Remotely sensed burned area products such as the MODIS-derived monthly 500-m resolution MCD64A1v61 burned area product (Giglio et al., 2015) provide valuable information on circumboreal burned area extent, seasonality and trends, but are only available since 2000 (Kurbanov et al., 2022). This short time series makes it difficult to detect trends in circumboreal wildfire due to the region's long wildfire-return intervals (Baltzer et al., 2021; Burrell et al., 2022) and high interannual variability in burned area (Jones et al., 2022).

An attempt has been made to extend circumboreal burned area products into the pre-MODIS era using observations from the Advanced Very High Resolution Radiometer (AVHRR) sensor flown on the NOAA POES satellites (1979–2022) (Oton et al., 2019, Oton et al. 2021a). However, the accuracy of that AVHRR burned area dataset, termed FireCCILT11, has been questioned (Giglio and Roy, 2020; Giglio et al., 2022), and it ends in 2018 due to the drift of NOAA-19's orbit (Roger et al., 2023). That drift greatly changes the sensor solar zenith angle of observation (SZA) due to changes in sensor overpass times (Dech et al., 2021), likely resulting in the creation of spurious burned area trends (Giglio and Roy, 2022). However, whether trends in the FireCCILT11 dataset are spurious may depend on geographic and temporal extent of analysis (Giglio and Roy, 2022), and some studies report robust results (Pullabhotla et al., 2023; Descals et al., 2022) while others report problems (Giglio and Roy, 2023).

We opted to develop, apply, and evaluate a new burned area algorithm designed for AVHRR data that is based on statistical time-series analysis. Statistical time-series analysis is an established and effective tool for disturbance detection using remotely sensed datasets, with the LandTrendr (Kennedy et al., 2010), Continuous Change Detection and Classification (CCDC) (Zhu et al., 2012), and Breaks for Additive Season and Trend (BFAST) (Verbesselt et al., 2010) algorithms used to track environmental disturbance the world over (Watts and Laffan, 2014; Pasquarella et al., 2022; Zhu, 2017). An advantage of statistical time-series models is the ability to explicitly account for known sources of variation, such as trends in SZA, within remotely sensed time series (Ives et al., 2021). This makes statistical time-series analysis an effective tool for remotely sensed change detection (Kennedy et al., 2010; Zhu and Woodcock, 2014) and thus a potentially effective method for burned-area mapping with AVHRR data.

We used our 1983–2020 burned area maps to (a) determine the net changes in burning over time, and (b) test if there were statistically significant trends. By definition, all significant trends are also changes, but not all changes are significant trends. That is especially true for boreal forests due to their large interannual variability in burned area (Jain et al., 2017; Jones et al., 2022) which can mean that even fairly large changes, if they occur only in a few extreme years, may not constitute statistically significant trends. That does not mean that changes caused by extreme years are not real or not biologically important, which is why reporting changes is important. However, it is also important to test for the statistical significance of trends because significance suggests that similar increases are likely to continue in the future. Changes and statistically significant trends thus provide complementary information (Ratajczak et al., 2018).

Here, we map circumboreal burned area annually from 1983 to 2020 and analyze changes and trends in burned area. Our objectives were to:

1. Develop a new burned area algorithm for AVHRR data that accounts for known problems related to SZA and sensor differences
2. Assess the accuracy of our algorithm by testing it with MODIS data, and to compare our burned area maps with other datasets
3. Summarize net change in burned area between the 1980s and the 2010s across the circumboreal region and within ecoregions
4. Test for significance of trends of annual burned area totals

2. Methods

2.1. Methodological Overview

Our burned area algorithm is based on autoregressive time-series analysis and accounts for both the differences in observations among sensors and change in solar zenith angle due to satellite drift in the AVHRR Long Term Data Record (LTDR) archive. We mapped a pixel as burned in a given year where there was a significant time-series residual, and both burn and greenness indices surpassed pre-defined thresholds. For burned pixels, we estimated subpixel burned area using models relating time-series residuals to subpixel burn fractions from reference datasets. To examine how sensor and spectral index affected algorithm performance, we also applied our burned area mapping algorithm to the 5-km MODIS MOD09CMGv061 dataset and analyzed the Burned Area Index (Chuvieco et al., 2002), Normalized Burn Ratio (Key and Benson, 2006), Global Environmental Monitoring Index (Pinty and Verstraete, 1992), and Enhanced Vegetation Index (Didan, 2015) spectral indices. We evaluated the accuracy of our burned area algorithm by comparing it to the MODIS MCD64A1v61 burned area dataset, AVHRR-based FireCCILT11 burned area dataset, joint US Forest Service and Department of Interior Monitoring Trends in Burn Severity (MTBS) fire perimeters for Alaska, and National Research Council (NRC) fire perimeters for Canada. Finally, we summarized changes and tested for significant trends in burned area using a second autoregressive time series analysis (Supplement 1).

2.2. Study area

Our study area included all of the boreal forests of North America and Eurasia, which span 23 of the World Wildlife Fund global terrestrial ecoregions Olson et al., 2001. Eurasia's boreal forests are primarily composed of larch (*Larix gmelinii*, *L. cajanderi*, *L. sibirica*) and Scots pine (*Pinus sylvestris*), which are adapted to frequent low-severity ground fires (Kharuk et al., 2021). North American boreal forests are mainly composed of Jack pine (*Pinus banksiana*), white spruce (*Picea glauca*) and black spruce (*Picea marina*), which are adapted to infrequent, high-severity crown fire (Wirth, 2005).

2.3. Data

2.3.1. AVHRR and MODIS satellite data

The Advanced Very High Resolution Radiometer Long Term Data Record provides the longest record of global, daily, multispectral satellite observations (1982-Present) (Dech et al., 2021) and are available with atmospheric and BRDF corrections (Vermote et al., 2022). Beginning in 2022, the LTDR project replaced post-2013 observations made by NOAA-19 with those made by the European Space Agency's MetOp-B satellite, extending the LTDR archive to the present day (Roger et al., 2023; LAADS, 2022). The September 1994 failure of NOAA-11's AVHRR sensor means that only a partial record of observations exists for that

year, so we did not report burned area for 1994. The MODIS sensors aboard NASA's Terra and Aqua satellite constellation provide two decades (2000 – present) of daily, global, multispectral observations. The MOD09CMGv061 surface reflectance product and the AVHRR LTDR dataset have identical resolution and projections, allowing direct comparison of resulting burned area maps

Effective cloud masking is needed for accurate burned area mapping (Lizundia-Loiola et al., 2020). The AVHRR LTDR and MOD09CMGv061 each have quality assurance (QA) flags indicating cloud, water, snow, and invalid observations. While the MOD09CMGv061 QA bitmasks are of sufficient quality for burned area mapping (Giglio et al., 2015), additional preprocessing of the AVHRR LTDR is required (Oton et al. 2021a), and so we implemented the cloud masking procedure outlined in Oton et al. (2021a) along with a NIR band threshold (Table S2).

2.3.2. Growing Season Burn Index Composites

Multispectral satellite observations can detect charcoal (Martin et al., 2006), enabling burned area mapping (Giglio et al., 2015, Oton et al. 2021a). AVHRR LTDR data can map burned area via the Burned Area Index (BAI) (Chuvieco et al., 2002, Oton et al. 2021a):

$$\boldsymbol{BAI} = \frac{1}{(\mathbf{0.1} - \boldsymbol{p}_{red})^2 + (\mathbf{0.06} - \boldsymbol{p}_{NIR})^2} \quad (1)$$

where $\boldsymbol{p}_{NIR}$ and $\boldsymbol{p}_{red}$ are near-infrared and red surface reflectance, respectively.

MODIS's additional shortwave infrared (SWIR) bands allows calculating the Normalized Burn Ratio (NBR) (Key and Benson, 2006):

$$\boldsymbol{NBR} = \frac{(\boldsymbol{p}_{NIR} - \boldsymbol{p}_{SWIR})}{(\boldsymbol{p}_{NIR} + \boldsymbol{p}_{SWIR})} \quad (2)$$

where $\boldsymbol{p}_{SWIR}$ is shortwave-infrared surface reflectance.

We mapped circumboreal burned area using annual growing-season BAI and NBR composites created from daily AVHRR LTDR (1982–2021) and MODIS MOD09CMGv061 (2000−2021) data. The BAI has a positive non-linear relationship with burned area, so differencing post and pre burn observations identifies burned area occurrence. We created annual BAI composites by differencing annual 90th and 10th percentile BAI values to capture post and pre burn conditions. We then implemented a $\log_{10}(x + 1)$ transformation on annual differenced BAI values to account of the BAI's non-linear response to burning. In contrast, NBR exhibits an inverse relationship with burned area, and so we selected the annual 10th percentile NBR values to highlight burned areas. We chose to use the annual 10th percentile daily NBR value instead of seasonally differenced daily index values because this method reduced omission errors in burned area mapping observed in initial tests.

2.3.3. Growing season vegetation index composites

Vegetation indices created from multispectral imagery are useful for assessing vegetation health and disturbance (Fensholt and Proud, 2012; Baumann et al., 2014; Cortes et al., 2021), and can complement burned area indices. The Global Environmental Monitoring Index (GEMI) (Eq. 3) was developed to reduce the influence of atmospheric contamination and high solar zenith angles in AVHRR data (Pinty and Verstraete, 1992):

$$\boldsymbol{GEMI} = \boldsymbol{\eta}^*(\mathbf{1} - \mathbf{0.25}^*\boldsymbol{\eta}) - \left(\frac{\boldsymbol{p}_{red} - \mathbf{0.125}}{\mathbf{1} - \boldsymbol{p}_{red}}\right) \quad (3)$$

$$\boldsymbol{\eta} = \frac{(\mathbf{2}^*(\boldsymbol{p}_{NIR}^2 - \boldsymbol{p}_{red}^2) + \mathbf{1.5}^*\boldsymbol{p}_{NIR} + \mathbf{0.5}^*\boldsymbol{p}_{red})}{\boldsymbol{p}_{NIR} + \boldsymbol{p}_{red} + \mathbf{0.5}}$$

Valid GEMI values range from 0 to 1 with higher values indicating more vegetation.

The MODIS sensor's higher spectral resolution enables calculation of the Enhanced Vegetation Index (EVI) (Eq. 4) (Didan, 2015), which reduces effects of soil brightness and saturation (Sobrino and Julien, 2013):

$$\boldsymbol{EVI} = \mathbf{2.5}^*\frac{\boldsymbol{p}_{NIR} - \boldsymbol{p}_{red}}{\boldsymbol{p}_{NIR} + \mathbf{6}^*\boldsymbol{p}_{red} - \mathbf{7.5}^*\boldsymbol{p}_{blue} + \mathbf{1}} \quad (4)$$

Where $\boldsymbol{p}_{blue}$ is blue reflectance. Valid EVI values range from −0.2 to 1 with higher values representing more vegetation.

To track changes in vegetation condition caused by burning, we calculated daily GEMI and EVI from daily AVHRR LTDR (1982–2021) and MODIS MOD09CMGv061 (2000–2021) surface reflectance data, respectively. We then aggregated these to annual growing season "greenness" composites by selecting the 90th percentile greenness value to reduce noise (Li et al., 2019). We detected burned areas by tracking standardized interannual change in annual 90th percentile AVHRR GEMI and MODIS EVI data (see below).

The compositing method of selecting the 90th percentile greenness pixel value for each year leads to a potential artifact: because burning reduces greenness, selecting the 90th percentile greenness pixel value typically excludes burn signatures from the year that burning occurs. Due to this lagged response, we calculated annual change for year $t - 1$ to year t by subtracting the value for year $t + 1$ from year t. However, if burning occurs prior to a given year's first available observations, then this method of calculation would cause the burn signature to appear between years $t - 1$ and t, thus preventing burning from being detected. Therefore, to account for this variability in burn signature occurrence, we applied a moving window operation (Supplement 3) to select the greatest standardized decrease in 90th percentile vegetation index value between the intervals of $t - 1$ to t and t to $t + 1$, and used this value for both intervals in the final product. Due to this moving window operation, we could not map burned area for the last year (2021) of the AVHRR and MODIS time series used in our analysis.

2.4. Geographic standardization of datasets

The AVHRR LTDR archive is an aggregate of observations recorded by eight different sensors over four decades (Vermote et al., 2022). Changes in sensor calibration and design can cause systematic differences in observations (Dech et al., 2021). Standardizing pixel values controls for these systematic differences (Oton et al., 2019, Oton et al. 2021a). Therefore, we standardized all datasets by year and continental region (Eq. 5):

$$\boldsymbol{z} = \frac{\boldsymbol{X} - \boldsymbol{\mu}}{\boldsymbol{\sigma}} \quad (5)$$

where $\boldsymbol{\mu}$ and $\boldsymbol{\sigma}$ represent the mean and standard deviation of pixel values for a given year and geographic region, $\boldsymbol{X}$ represents the pixel value, and $\boldsymbol{z}$ represents the pixel value's z-score. For consistency, we applied this procedure also to our MODIS datasets even though there were no changes among sensors over time.

2.5. Burned pixel detection with autoregressive time series analysis

Our burned area algorithm examines full time series of annual BAI and NBR index values, and decides if the residual of a given year is so great that it likely represents a burned area. Satellite image time series exhibit temporal autocorrelation (Box et al., 1994; Ives et al., 2021), and therefore we developed our burned area detection method based on autoregressive time-series analysis. Our burned area algorithm includes three steps: (i) fit an AR(1) linear model to our annual burn index time series and conduct binary detection of burned versus non-burned pixels using a studentized residuals test; (ii) spatially filter burned area detections to mitigate commission errors due to geolocation errors; and (iii) estimate subpixel burned area using a model relating time series analysis residuals to reference burned pixel fractions. Because autoregressive models use prior observations as a predictor variable, burned area cannot be mapped for the first year of either the AVHRR (1982) or MODIS (2000) archives.

The orbital drift of the NOAA POES satellites that carried the AVHRR sensors requires accounting for the influence of changing solar zenith angle of observation (SZA) on BAI. To our knowledge, no relationship between BAI and SZA has been published. However, because the BAI measures the similarity of red and near-infrared (NIR) observations to the spectral signature of charcoal (a dark surface), progressive darkening of these bands by increasing SZA increases BAI values. To correct for SZA, we selected a 3rd order polynomial model (Eq. 6) based on an initial analysis and model rankings by the Bayesian Information Criteria (BIC) (Fig. 1). Thus, our pixel-based polynomial AR(1) temporal autoregressive model accounts for (a) temporal autocorrelation, (b) solar zenith angle, (c) time trends in annualized burn index time series which may occur due wildfire effects (Chuvieco et al., 2002), and (d) sensor-based differences in observations by standardizing inputs:

$$\boldsymbol{y_t} = \boldsymbol{\beta_0} + \boldsymbol{\beta_1}(\boldsymbol{y_{t-1}}) + \boldsymbol{\beta_2}(\boldsymbol{c_t}) + \boldsymbol{\beta_3}(\boldsymbol{SZA_t}) + \boldsymbol{\beta_4}(\boldsymbol{SZA_t^2}) + \boldsymbol{\beta_5}(\boldsymbol{SZA_t^3}) + \boldsymbol{\epsilon_t} \quad (6)$$

where $\boldsymbol{y_t}$ represents the burn index value at time $\boldsymbol{t}$, $\boldsymbol{\beta_0}$ the fitted intercept, $\boldsymbol{\beta_1}$ the AR(1) autoregressive correlation between current and prior year's burn index values, $\boldsymbol{\beta_2}$ the fitted burn index time trend, $\boldsymbol{c_t}$ the current year $\boldsymbol{t}$, $\boldsymbol{\beta_3}$, $\boldsymbol{\beta_4}$, and $\boldsymbol{\beta_5}$ the coefficients for the 3rd-order polynomial relationship between current burn index value and solar zenith angle, $\boldsymbol{SZA_t}$ the solar zenith angle of the observation corresponding to the 90th percentile burn index values, and $\boldsymbol{\epsilon_t} \sim \boldsymbol{N}(\boldsymbol{0}, \boldsymbol{\sigma^2})$ random error. We did not include SZA in our MODIS burned area detection algorithm because MODIS is not afflicted by substantial orbital drift (Chander et al., 2010).

We created annual binary burned area maps by applying a studentized residuals test to the fitted burn index (e.g. BAI, NBR) time-series models. Specifically, pixels were classified as burned if (a) their burn index time-series residual was significant ($\alpha = 0.1$), and (b) they exceeded a 1/3rd pixel burn threshold in standardized burn index, standardized Δ burn index, and standardized Δ in vegetative index (e.g. GEMI, EVI) values (Fig. 2). We defined these 1/3rd pixel burn thresholds by extracting each index value to its corresponding reference pixel burn fraction value, excluding pixels where no burning occurred. We then aggregated these extracted index values into burn fraction quartiles and averaged each index's values within the 0.25–0.5 burn fraction quartile. We selected this conservative threshold to reduce false detections of burned areas. Additionally, by requiring burning to have a persistent effect on greenness for multiple years, we reduced the likelihood of commission errors due to ephemeral changes such as cloud shadow, observation error, or short-term flooding (Liu et al., 2023). We selected different pixel burn thresholds for AVHRR and MODIS datasets, and also for North American and Eurasian continental regions, to account for sensor differences and regional geographic standardization of datasets.

2.6. Spatial Filtering

Georegistration errors of approximately one pixel are common in AVHRR LTDR data (Key et al., 2019a), causing errors especially in pixels adjacent to waterbodies and other dark surfaces (White et al., 2018). To reduce commission errors in our burned area data caused by georegistration errors, we excluded binary burned pixel detections which did not have additional burned pixel detection within a 3 × 3 pixel window. Additionally, we removed burned pixel detections that contained water bodies within a 3 × 3 pixel window as indicated by the QA mask.

2.7. Subpixel burned area estimation

The coarse spatial resolution of AVHRR LTDR observations means many pixels are only partially burned (Oton et al., 2019), which is why we estimated subpixel burned area. We accomplished this by estimating subpixel burned area based on the magnitude of time-series residuals. We created subpixel burned area models by aggregating reference pixel burn fraction datasets into 5 % bins and regressing bin centers against corresponding averaged burn index time-series residuals (Fig. 3). The subsampling method used to create AVHRR LTDR observations (Franch et al., 2017) means that subpixel burning may only be partially detected (Giglio and Roy, 2020). As such, we selected for burned area signatures within time-series residuals by using only the top 50 % of positive residuals in each 5 % bin for BAI time series, and bottom 50 % of negative residuals for NBR time series. We then predicted subpixel burned area for both pixels flagged as burned and pixels within their surrounding 3 × 3 pixel window to capture partially burned pixels along fire perimeters. We estimated subpixel burned area in the same way for both AVHRR and MODIS data, but parameterized separate models for each continent and dataset.

2.8. Reference burned area datasets and burned area dataset validation

The combined MTBS and NRC Landsat-based burned area archive (MTBS, 2022; NRC, 2024) provide multidecadal (1984–2020) medium-resolution maps of burned area for North American boreal forests. No equivalent Landsat-based dataset exists for Eurasia, but the 500-m MODIS-based burned area data (MCD64A1v61, 2001–2020) (Giglio et al., 2015) is available in both continents. Accordingly, we validated our 5-km resolution AVHRR and MODIS burned area data with the 30-m Landsat burned area data for North American boreal forests, and the 500-m MODIS burned area data for both North America and Eurasia. The coarser resolution of MODIS data means that the MCD64A1v61 exhibits greater burned area mapping errors than Landsat-derived datasets (Boschetti et al., 2004; Boschetti et al., 2019). To evaluate the

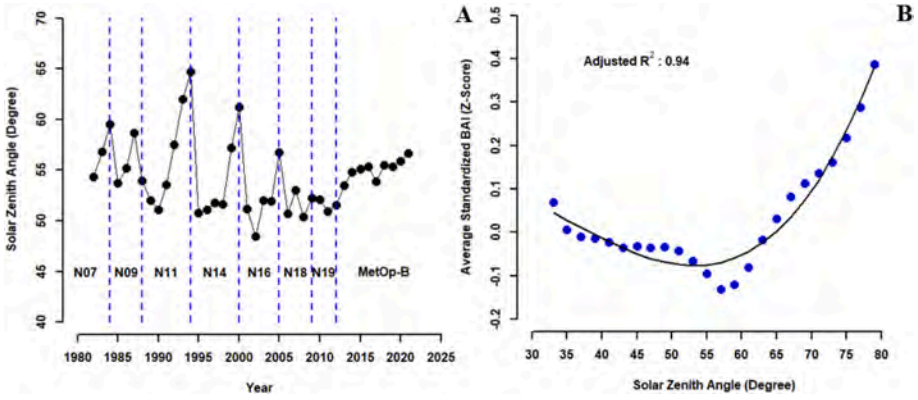

Fig. 1. Trends in solar zenith angle of observation over the lifetime of each NOAA POES and ESA MetOp satellite used to collected AVHRR data (A). Progressive orbital drift of each satellite results in increasing average solar zenith angle of observation, which can positively bias burned area index values (B). The positive relationship between solar zenith angle of observation and burned area index can be approximated using a third order polynomial relationship between standardized log10 (90th – 10th percentile) burned area index and the 90th percentile burned area index solar zenith angle of observation.

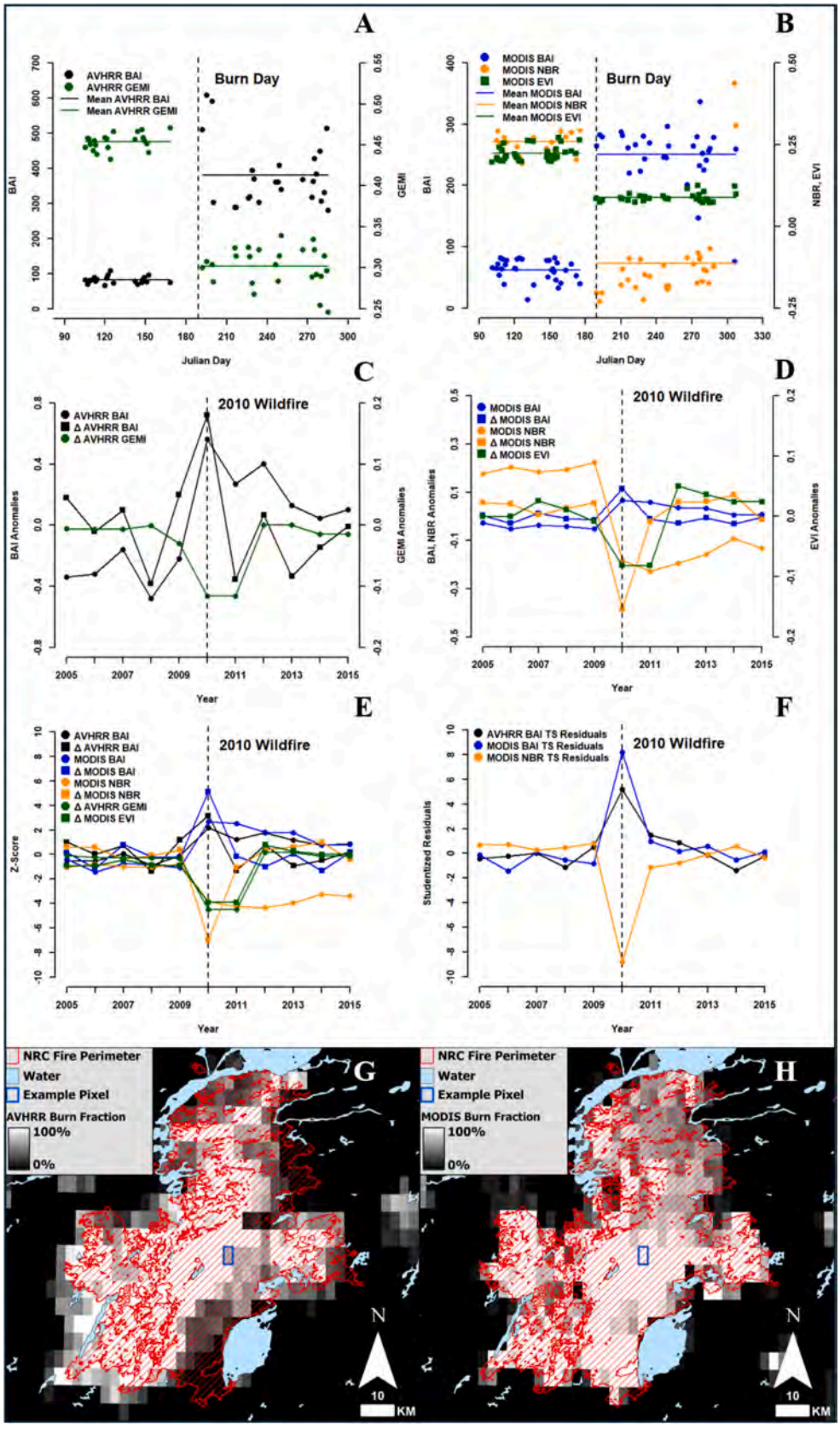

(caption on next page)

Fig. 2. Burned area mapping procedure (A-F) demonstrated for an example 2010 North American burned pixel mapped using AVHRR LTDR (G, purple outline) and MODIS CMG (H, purple outline) daily observations. Extracted time series of AVHRR (A) and MODIS (B) daily spectral indices demonstrate the response of each index to burning the year of wildfire occurrence. These daily AVHRR (C) and MODIS (D) spectral indices are then annualized to highlight the occurrence of burning, enabling burned area detection. These composites are then standardized by year and continental region to account for sensor-based interannual biases and used for autoregressive time series analysis (E). Finally, the resulting time series analysis residuals (F) are used for both burned area detection and subpixel burn fraction estimation, resulting in AVHRR (G) and MODIS (H) based burned area fraction maps. (For interpretation of the references to colour in this figure legend, the reader is referred to the web version of this article.)

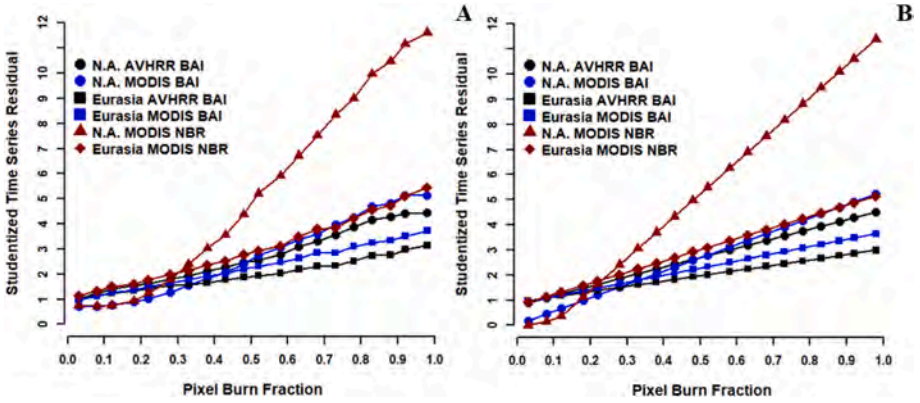

Fig. 3. Relationship between time series analysis residuals and subpixel burned area fraction corresponding to each geographic region, sensor, and burn index used in analysis (A) used to create models used for subpixel burned area estimation (B). The absolute value of NBR time series analysis residuals is displayed for direct comparison between models.

effects of the MCD64A1v61 mapping errors on the validation of our burned area datasets, we compared validation metrics found with MTBS/NRC and MCD64A1v61 datasets for those years where both were available (North America, 2001–2020). We resampled those data to annual 5-km resolution pixel burn fractions (0–100 %) to match AVHRR's resolution.

We validated our AVHRR and MODIS burned area datasets using four metrics: (a) burned pixel detection rate, (b) User's and Producer's accuracies (c) subpixel burn fraction estimate versus reference burned area data, and (d) annual mapped burned area Pearson's correlation with reference annual burned area datasets. We determined the burned pixel detection rate by reclassifying reference pixel burn fraction datasets into five classes: Unburned, 1–25 %, 26–50 %, 51–75 %, and 76–100 % Burned. We then converted our subpixel burned area dataset to a binary burned area mask and calculated detection rates for each class and burned area dataset. We also used these binary burned area masks to calculate User's and Producer's accuracies relative to reference burned area datasets, and implemented corresponding area estimate corrections based on these metrics (Olofsson et al., 2014). Specifically, we implemented area estimate corrections for our North American and Eurasian burned area datasets based on User's and Producer's accuracies relative to the Landsat-based MTBS/NRC (1984–2020) and MCD64A1v61 (2001–2020) datasets respectively, because they are the best validated datasets for each region.

We evaluated subpixel burn fraction estimate accuracy by aggregating reference pixel burn fraction datasets into 5 % bins and extracting corresponding subpixel burn fraction estimates from each of our burned area dataset. We then averaged each dataset's subpixel burned area estimates within each bin. We used the resulting curves to estimate subpixel burn fraction accuracy by calculating each curve's mean absolute percent error (MAPE) with reference burned area fraction. Finally, we used Pearson's correlation to quantify agreement in trends of total mapped annual burned area for each continental region compared to Landsat-based MTBS/NRC and MCD64A1v61 reference burned area datasets.

2.9. Analysis of net decadal change in burned area

A topic of major interest in climate science is whether climate change is increasing circumboreal burning (Reich et al., 2022; Gauthier et al., 2015; Astrup et al., 2018). However, due to high interannual variability in wildfire activity, substantial absolute changes in burned area can occur even when there is no statistically significant trend. To quantify the net change in burned area for each time series, we summed the total burned area for the first ten years of our data (1983–1992, hereafter the 1980s) and for the last ten years (2011–2020, the 2010s) and calculated the resulting change both in percentage points (i.e., how much more or less area of a given ecoregion burned) and as a percent change (akin to a growth rate).

2.10. Analysis of significant trends in burned area

After mapping burned area for each year using both AVHRR and MODIS data, we examined if there were trends in total burned area in (a) the total boreal biome in each of the two continents, and (b) each boreal ecoregion. We chose to test for ecoregion-scale burned area trends to both aid with comparison between our burned area datasets and reference burned area datasets, and to enable comparison of our observed burned area trends with previously published regional studies. For this second trend analysis, we parameterized different models for biome scale and ecoregion scale analyses. To test for biome-scale trends in annual burned area, we parameterized a second order (AR(2)) Phylogenetic Generalized Linear Mixed Model (PGLMM) (Ives and Helmus, 2011; Bosch and Ives, 2023) which treats ecoregion of wildfire occurrence as a random effect while also incorporating their geographic correlations in place of phylogenetic correlations (Eq. 7). We used the PGLMM for biome-scale analyses because it both incorporates ecoregion-scale information on and accounts for spatial correlation in location of burning, thus retaining greater information on burned area change than an analysis of regional summaries (Ives and Helmus, 2011, Bosch and Ives, 2023).

In addition to affecting our burn indices directly, an increasing SZA is also related to a progressive loss of sensitivity to burning exhibited by the AVHRR sensor over its operational lifetime (Giglio and Roy, 2020).

This is because average SZA of observation increases with satellite age (Dech et al., 2021), which is correlated to reduced sensor performance due to progressive mechanical degradation. That is why we included the SZA of 90th percentile BAI observation averaged by geographic region of analysis as a model covariate in both our biome and ecoregion scale models.

$$\boldsymbol{BA}_{i,t} = \beta_0 + \beta_1\left(\boldsymbol{BA}_{i,t-1}\right) + \beta_2\left(\boldsymbol{BA}_{i,t-2}\right) + \beta_3\left(\boldsymbol{SZA}_{i,t}\right) + \beta_4(\boldsymbol{c}_t) + \eta_i + \epsilon_{i,t} \quad (7)$$

where $\boldsymbol{BA}_t$ represents total burned area in ecoregion $\boldsymbol{i}$ in year $\boldsymbol{t}$, β_0 the fitted intercept, β_1 the AR(1) autoregressive correlation between years $\boldsymbol{t}$ and $\boldsymbol{t-1}$ annual burned area, β_2 the AR(2) autoregressive correlation between years $\boldsymbol{t}$ and $\boldsymbol{t-2}$ annual burned area, β_3 the relationship between current year $\boldsymbol{t}$ burned area and solar zenith angle of observation, $\boldsymbol{SZA}_t$ the solar zenith angle of observation for 90th percentile BAI values for year $\boldsymbol{t}$ averaged by geographic region of analysis, β_4 the fitted annual burned area time trend, $\boldsymbol{c}_t$ the current year $\boldsymbol{t}$, η_i represents the random effect of ecoregion $\boldsymbol{i}$ which follows a multivariate normal distribution $\boldsymbol{N}(\mathbf{0},\mathbf{V}_{\mathbf{geo}} + \mathbf{G})$ where $\mathbf{V}_{\mathbf{geo}}$ represents the spatial covariance matrix between ecoregions and $\mathbf{G}$ represents the random effects covariance matrix, and $\epsilon_{i,t} \sim \boldsymbol{N}(\mathbf{0},\sigma^2)$ represents random error.

For ecoregion-scale analyses, we parameterized a second order (AR (2)) linear model (Eq. 8). We selected second order autoregressive models for both biome and ecoregion scale analyses to account for the influence of temporal autocorrelation and cyclic atmospheric processes such as the Arctic Oscillation and Pacific-North American pattern on burned area (Justino et al., 2022; Bonsal et al., 2017). Boreal forests experience intermittent years of high wildfire activity (Coops et al., 2018), that may appear as outliers in burned area time series, necessitating that annual burned area is normalized (Grillakis et al., 2022). Accordingly, we applied a log10(x + 1) transformation to annual burned area datasets prior to time-series analyses.

$$\boldsymbol{BA}_t = \beta_0 + \beta_1(\boldsymbol{BA}_{t-1}) + \beta_2(\boldsymbol{BA}_{t-2}) + \beta_3(\boldsymbol{SZA}_t) + \beta_4(\boldsymbol{c}_t) + \epsilon_t \quad (8)$$

where $\boldsymbol{BA}_t$ represents total burned area in a given ecoregion in year $\boldsymbol{t}$, β_0 the fitted intercept, β_1 the AR(1) autoregressive correlation between years $\boldsymbol{t}$ and $\boldsymbol{t-1}$ annual burned area, β_2 the AR(2) autoregressive correlation between years $\boldsymbol{t}$ and $\boldsymbol{t-2}$ annual burned area, β_3 the relationship between current year $\boldsymbol{t}$ burned area and solar zenith angle of observation, $\boldsymbol{SZA}_t$ the solar zenith angle of observation for 90th percentile BAI values for year $\boldsymbol{t}$ averaged by geographic region of analysis, β_4 the fitted annual burned area time trend, $\boldsymbol{c}_t$ the current year $\boldsymbol{t}$, and $\epsilon_t \sim \boldsymbol{N}(\mathbf{0},\sigma^2)$ random error.

3. Results

3.1. Burned area mapping algorithm performance

Our burned area mapping algorithm worked well, with both our AVHRR and MODIS-based burned area datasets showing high burned pixel detection rate, Pearson's correlation, subpixel burned area accuracy, and satisfactory User's and Producer's accuracies when compared with reference burned area datasets (Table 1, Supplement 4). While in all cases our MODIS-based burned area datasets exhibited higher agreement with reference burned area datasets than our AVHRR-based ones, this is to be expected given the spatial and spectral limitations of AVHRR data (Giglio and Roy, 2020). Within North American boreal forests, our AVHRR-based burned area dataset detected 73 % of heavily burned pixels (>75 % burned), achieved User's and Producer's accuracies of 42.5 % and 54.2 %, and exhibited a Pearson's correlation of 0.85 with the 36-year MTBS/NRC archive. Agreement between our AVHRR-based burned area dataset and the MCD64A1v61 archive was similarly high (71.1 %, User's Accuracy = 37.4 %, Producer's Accuracy = 55.5 %, cor. = 0.75), and increased for our MODIS-based BAI (83 %, User's Accuracy = 66.1 %, Producer's Accuracy = 66.2 %, cor. = 0.84) and NBR burned area datasets (91.6 %, User's Accuracy = 61.0 %, Producer's Accuracy = 76.1 %, cor. = 0.94). Within Eurasian boreal forests, our AVHRR-based burned area dataset detected 51.1 % of heavily burned pixels, achieved User's and Producer's accuracies of 44.9 % and 33.6 %, and exhibited a Pearson's correlation of 0.77 with the MCD64A1v61 archive. As with our North American burned area datasets, agreement increased for our MODIS-based BAI (62.3 %, User's Accuracy = 66.0 %, Producer's Accuracy = 42.1 %, cor. = 0.77) and NBR burned area datasets (58.9 %, User's Accuracy = 57.3 %, Producer's Accuracy = 38.7 %, cor. = 0.78). These results show that while the AVHRR-based BAI datasets are suitable for burned area mapping using our algorithm, MODIS-based BAI and NBR datasets generally perform better, which is to be expected (Guo et al., 2024; Giglio and Roy, 2020).

Comparison of North American boreal forests burned pixel detection rates calculated using MTBS/NRC and MCD64A1v61 validation datasets for overlapping years (2001–2020) highlights the impact of MCD64A1v61 mapping errors (Boschetti et al., 2019) on the validation of our burned area datasets. While the difference between MTBS/NRC

Table 1
Burned area dataset accuracy assessment metrics representing burned pixel detection rate by subpixel burn fraction quantile (1–100 %), BA ratio (ratio of average annual mapped burned area to average annual reference burned area), Pearson's correlation between total annual mapped burned area and reference burned area datasets, and Producer and User accuracies for Eurasian and North American continental regions.

Dataset	Region	1–25 %	26–50 %	51–75 %	76–100 %	Reference Dataset	BA Ratio	Pearson Correlation	Producer's Accuracy	User's Accuracy
AVHRR BAI	N.A.	11.0	29.4	51.3	73.0	MTBS/NRC (1984–2020)	0.66	0.85	54.2 %	42.5 %
AVHRR BAI	N.A.	10.5	28.6	49.5	72.0	MTBS/NRC (2001–2020)	0.64	0.72	54.3 %	42.3 %
MODIS BAI	N.A.	13.0	39.3	65.0	81.1	MTBS/NRC (2001–2020)	0.67	0.87	65.1 %	75.5 %
MODIS NBR	N.A.	14.4	49.6	79.2	92.0	MTBS/NRC (2001–2020)	0.63	0.92	76.2 %	68.9 %
AVHRR BAI	N.A.	18.7	38	52.5	71.1	MCD64A1v61 (2001–2020)	0.79	0.75	55.5 %	37.4 %
MODIS BAI	N.A.	23.4	48.9	66.1	83	MCD64A1v61 (2001–2020)	0.83	0.84	66.2 %	66.1 %
MODIS NBR	N.A.	28.8	58.6	78.5	91.6	MCD64A1v61 (2001–2020)	0.78	0.94	76.1 %	61.0 %
AVHRR BAI	Eurasia	7.6	17.8	28.8	51	MCD64A1v61 (2001–2020)	0.85	0.77	33.6 %	44.9 %
MODIS BAI	Eurasia	8.4	23.1	38.4	62.3	MCD64A1v61 (2001–2020)	0.80	0.77	42.1 %	66.0 %
MODIS NBR	Eurasia	8.4	20.5	33.4	58.9	MCD64A1v61 (2001–2020)	0.76	0.78	38.7 %	57.3 %

and MCD64A1v61derived burned pixel detection rates was between −3 % to 1 % for moderately (51–75 %) and heavily (76–100 %) burned pixels, MTBS/NRC had 9–14 % fewer lightly burned (1–25 %, 26–50 %) pixels than the MCD64A1v61. This suggests that the MCD64A1v61 is omitting smaller fires and therefore positively biasing MCD64A1v61-based validation of our burned area datasets in both North American and Eurasian boreal forests.

Estimating subpixel burn fraction with AVHRR LTDR data is challenging due to the subsampling method used to create AVHRR LTDR observations which results in only 33 % of a pixel being observed (Vermote et al., 2022; Dech et al., 2021). Given this limitation, our AVHRR-based burned area datasets estimated subpixel burned area effectively, with our North American burned area dataset exhibiting a mean absolute percent error (MAPE) of 68.91 % with the 36-year MTBS/NRC burned area reference dataset. MAPE was greater (90.65 %) when compared to the MCD64A1v61 archive and decreased for our MODIS-based BAI (56.68 %) and NBR (57.79 %) burned area datasets. Within Eurasian boreal forests, our AVHRR-based burned area dataset exhibited a MAPE of 122.45 % with the MCD64A1v61 archive which likewise decreased for our MODIS-based BAI (79.67 %) and NBR (68.6 %) burned area datasets. These results show that while our method of estimating subpixel burned area does so effectively and that our AVHRR-based burned area datasets provide valuable information on subpixel burned area, our MODIS-based burned area datasets generally do so more accurately, which is to be expected.

3.2. Influence of solar zenith angle of observation on AVHRR burned area datasets

Increasing solar zenith angle of observation caused by the drifting orbits of the NOAA POES satellites can result in burned area mapping artifacts (Giglio and Roy, 2022), which makes it important to check for these artifacts (Giglio and Roy, 2020). Within North American boreal forests, MTBS/NRC derived annual (1984–2020) heavily burned (>75 % burned) pixel detection rate exhibited a mildly significant ($p = 0.07$) negative relationship with averaged annual SZA of 90th percentile BAI observations, meaning that heavily burned pixels were less likely to be detected during high SZA-years. However, we observed no relationship within North American or Eurasian boreal forests when compared to MCD64A1v61 (2001–2020) derived reference products (Supplement 5). Inclusion of the polynomial relationship between SZA and 90th percentile BAI observation as covariates in BAI time series analysis reduced overclassification of burned area. This in turn increased Pearson's correlation between our North American AVHRR burned area dataset and the MTBS/NRC reference datasets by from 0.81 to 0.85 for the full time series (1984–2020), and from 0.87 to 0.93 for the pre-MODIS era (1984–2000) when high-SZA observations are more common (Dech et al., 2021). A corresponding analysis for Eurasia was unfortunately not possible due to the absence of pre-2000 reference datasets.

In additional tests we found that datasets excluding SZA as time series model covariates mapped a greater amount of burned area during high-SZA years (Supplement 5). Correspondingly, the magnitude of difference in mapped burned area was positively correlated with averaged SZA of the 90th percentile BAI observation for both North American ($r = 0.46$, $p < 0.01$) and Eurasian ($r = 0.59$, $p < 0.01$) burned area datasets. Finally, we found no significant relationship between average estimated AVHRR subpixel burned fraction and SZA of the 90th percentile BAI observation (Supplement 5).

3.3. Net change in burned area between the 1980s and 2010s

Based on our AVHRR datasets we mapped an average of 2.76 and 5.68 Mha·yr^{-1} of burned area for the full time series (1983–2020) within North American and Eurasian boreal forests, respectively (Figs. 4, 5). For the MODIS era alone, we mapped based on our AVHRR, MODIS BAI, and MODIS NBR datasets averages of 3.02, 3.10, 2.91 and 6.68, 6.27, and 5.97 Mha·yr^{-1} of burned area within North American and Eurasian boreal forests, respectively (Fig. 6). Wildfire burned 5.37 % of the circumboreal biome during the 1980s and 8.22 % during the 2010s, a percentage point increase of 2.85 % that corresponds to a proportional increase of 0.53, and represents 0.48 and 0.54 increases within North America and Eurasia, respectively (Table 2). Across circumboreal ecoregions, 18 ecoregions experienced a net increase and five experienced a net decrease in burned area over this timespan (Figs. 7). Furthermore, burning doubled within three ecoregions (Canadian Aspen Forests and Parkland Forests, Northern Cordillera Forests, Eastern Canadian Forests), tripled within three ecoregions (Yukon Interior Dry Forests, Northeast Siberian Taiga, Northern Canadian Shield Taiga), and quadrupled within one ecoregion (Muskwa Slave Lake Forests) in the 2010s compared to the 1980s (Table 2, Fig. 8). Finally, of the five ecoregions which experienced the greatest increases in burning in the

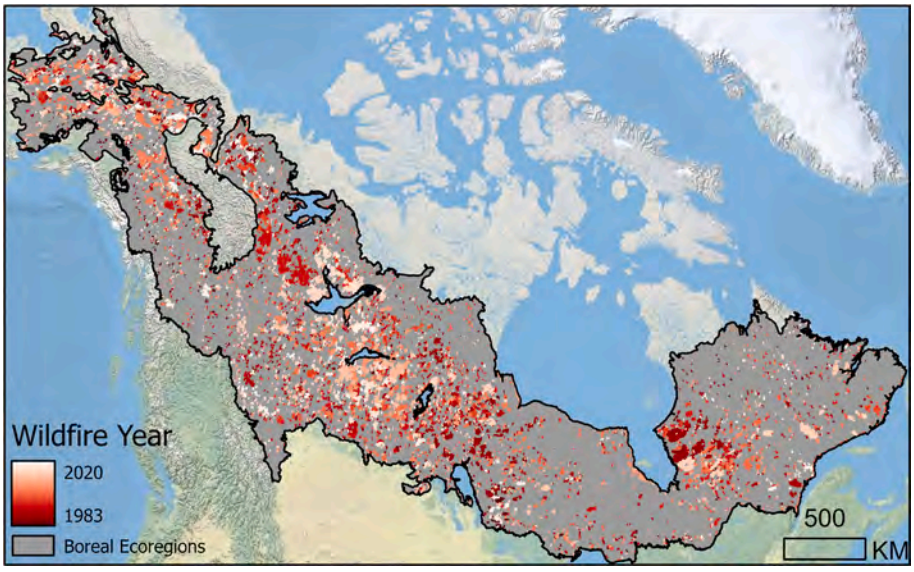

Fig. 4. Pixel burn year (1983–2020) mapped by our AVHRR burned area dataset for North American boreal region. The majority of mapped burned area is present within central and western North American boreal forests.

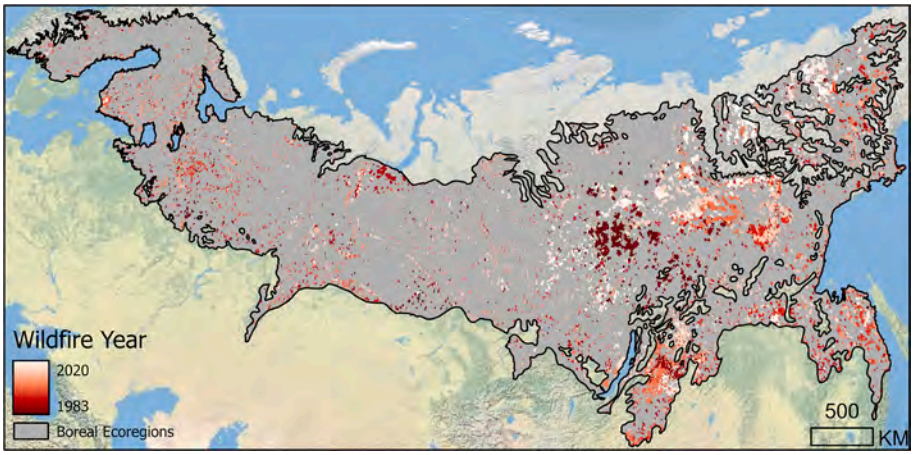

Fig. 5. Pixel burn year (1983–2020) mapped by our AVHRR burned area dataset Eurasian boreal region. The majority of mapped burned area is present within East Eurasian boreal forests.

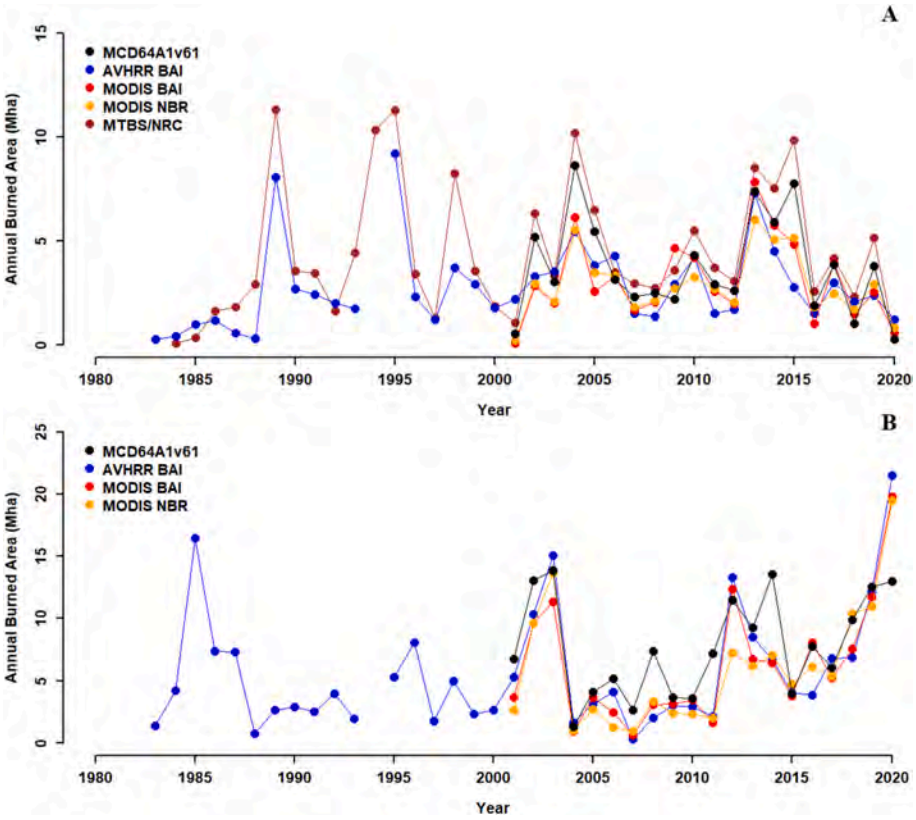

Fig. 6. Time series of annual AVHRR, MODIS, and reference burned area datasets for North American (A) and four east Siberian ecoregions (East Siberian Taiga, Northeast Siberian Taiga, Trans-Baikal Conifer Forests, and Okhotsk-Manchurian Taiga) comprising 90 % of burned area mapped in the MCD64A1v61 (2001–2020) reference dataset (B). Both time series exhibit high interannual variability in mapped annual burned area characteristic of boreal wildfire regimes.

2010s relative to the 1980s, four were located in North America and one in Eurasia.

3.4. Burned Area Trends

Across our 20 and 37-year AVHRR burned area datasets, respectively, we found a significant ($p = 0.09$) decreasing trend of −0.59 % yr^{-1} and suggested ($p = 0.12$) increasing trend of 0.24 %yr^{-1} in burned area across the North American boreal region (Table 3). Preliminary analyses also found a decreasing second-order trend ($p < 0.01$) across our 37-year AVHRR burned area dataset, which ends in 2020. We found the same second-order trend when analyzing the NRC annual burned area summaries (NRC, 2024) for the same 37 years as the AVHRR dataset. However, that second-order trend was no longer significant ($p > 0.1$) when analyzing NRC data up to 2023 that included the major fire year of 2023, which is why we did not investigate non-linear trends any further. These results align with those found across our 20-year MODIS-based BAI and NBR burned area datasets which showed non-significant decreases of −0.02 %yr^{-1} and -0.05 %yr^{-1} respectively. Within the Eurasian boreal region, we found a non-significant ($p = 0.72$) decrease of −0.39 %yr^{-1} and significant ($p = 0.10$) increasing trend of 0.56 % yr^{-1} in burned area across the same 20 and 36-year timespans

Table 2
AVHRR-based (1983–2020) circumboreal ecoregion level net change in annual burned area (BA).

Ecoregion	1983–1992 Total BA	2011–2020 Total BA	Percentage Point Change	Proportional Increase
	(% Ecoregion)	(% Ecoregion)	(% Ecoregion)	(ΔBA / 1983–1992 BA)
Alaska St Elias Range Tundra	2.81	1.36	−1.45	−0.52
Alberta British Columbia Foothills	2.15	3.23	1.08	0.50
Canadian Aspen Forests and Parklands Forests	2.52	5.96	3.44	1.37
Central Canadian Shield Forests	2.97	5.31	2.34	0.79
Eastern Canadian Forests	0.89	2.63	1.74	1.96
Eastern Canadian Shield Taiga	9.13	3.37	−5.76	−0.63
Interior Alaska Yukon Lowland Taiga	4.91	6.24	1.33	0.27
Interior Yukon Alaska Alpine Tundra	1.92	2.01	0.09	0.05
Mid Continental Canadian Forests	3.67	6.43	2.76	0.75
Midwestern Canadian Shield Forests	6.28	6.17	−0.11	−0.02
Muskwa Slave Lake Forests	1.88	8.33	6.45	3.43
Northern Canadian Shield Taiga	2.58	9.04	6.46	2.50
Northern Cordillera Forests	0.95	2.28	1.33	1.40
Northwest Territories Taiga	4.60	8.25	3.65	0.79
Southern Hudson Bay Taiga	1.49	2.08	0.59	0.40
Yukon Interior Dry Forests	1.29	4.23	2.94	2.28
East Siberian Taiga	9.76	13.92	4.16	0.43
Northeast Siberian Taiga	7.04	23.35	16.31	2.32
Okhotsk Manchu Taiga	3.72	6.41	2.69	0.72
Scandinavian and Russian Taiga	2.25	1.21	−1.04	−0.46
Trans Baikal Conifer Forests	8.76	11.44	2.68	0.31
Ural Montane Forests and Tundra	0.94	1.73	0.79	0.84
Western Siberian Taiga	4.36	3.92	−0.44	−0.10
North American Boreal Region	3.51	5.20	1.69	0.48
Eurasian Boreal Region	6.41	9.90	3.49	0.54
Circumboreal Region	5.37	8.22	2.85	0.53

respectively. Conversely however, this non-significant decrease in burned area across our 20-year AVHRR dataset did not agree with the non-significant ($p > 0.3$) increases in burned area of 1.13 %yr^{-1} and 1.14 %yr^{-1} found across our MODIS-based BAI, NBR burned area datasets respectively.

Among circumboreal ecoregions, we found that annual burned area significantly increased by 0.17 %yr^{-1} ($p = 0.02$), 0.13 %yr^{-1} ($p = 0.04$), 0.12 %yr^{-1} ($p = 0.09$), 1.07 %yr^{-1} ($p = 0.07$), 0.44 %yr^{-1} ($p = 0.1$), and 0.78 %yr^{-1} ($p = 0.05$) within the Canadian Aspen Forests and Parklands, Northern Cordillera Forests, Alberta British Columbia Foothills, Interior Alaska Lowland Taiga, Mid Continental Canadian Forests, and Northern Cordillera Forests ecoregions, respectively across our 37-year AVHRR burned area dataset (Fig. 9, Supplement 6). Additionally, annual burned area was suggested ($p = 0.13$) to have increased by 1.37 %yr^{-1} within the Northeast Siberian Taiga ecoregion over the same interval. Finally, we found annual burned area to have significantly ($p = 0.06$) decreased by 0.56 %yr^{-1} within the Eastern Canadian Shield Taiga ecoregion.

Comparison of ecoregion-level trends observed across our 20-year AVHRR, MODIS-based BAI and NBR datasets found good agreement. Across our 20-year AVHRR burned area dataset we found a significant ($\alpha = 0.1$) increasing trend of 0.29 %yr^{-1} within the Alberta British Columbia Foothills ecoregion that was also present within our MODIS BAI (0.15 %yr^{-1}) and NBR (0.28 %yr^{-1}) based burned area datasets. Additionally, we found a significant increasing trend of 0.34 %yr^{-1} within the Canadian Aspen Forests and Parkland Forests ecoregion across our 20-year AVHRR dataset that as omitted in our MODIS-BAI dataset (0.16 %yr^{-1}, $p = 0.34$) but present within our MODIS-NBR dataset (0.38 %yr^{-1}, $p = 0.03$). We found a significant decreasing trend in burned area within the Scandinavian and Russian Taiga ecoregion across our 20-year AVHRR dataset (−2.76 %yr^{-1}) that was also present in both our MODIS-BAI (−0.49 %yr^{-1}) and MODIS-NBR (−0.29 %yr^{-1}) datasets. Finally, we found a significant increasing trend in burned area within the Eastern Siberian Taiga ecoregion of 4.31 %yr^{-1} and 5.71 %yr^{-1} across our MODIS-BAI and MODIS-NBR datasets that was not present within our 20-year AVHRR dataset (3.70 %yr^{-1}, $p = 0.29$). This overall agreement in trends observed across our 20-year AVHRR and MODIS-based burned area datasets suggests that our AVHRR-based area burned area dataset, while constrained by the limitations of AVHRR data (Giglio and Roy, 2020), is consistent with those produced using better-validated sensors (MODIS) and provides useful information on burned area trends.

Comparison of ecoregion-scale burned area trends observed across our 20-year and 37-year burned area datasets yielded interesting results. Of the seven boreal ecoregions which experienced significant ($\alpha = 0.1$) (Alberta British Columbia Foothills, Canadian Aspen Forests and Parklands Forests, Interior Alaska Yukon Lowland Taiga, Mid Continental Canadian Forests, Northern Canadian Shield Taiga, Northern Cordillera Forests) or suggested (Northeast Siberian Taiga, $p = 0.13$) increasing trends in burned area over our 37-year AVHRR burned area dataset, only one (Alberta British Columbia Foothills) was also present in our 20-year AVHRR, MODIS-BAI, and MODIS-NBR dataset. This discrepancy highlights the challenge that high interannual variability in boreal burning poses to testing for significant trends with shorter-term (20 year) time series, and why developing multidecadal datasets is necessary.

While not all net changes in burning between the 1980s and 2010s resulted in significant ($\alpha = 0.1$) trends, in no case did an ecoregion experience a significant trend in annual burned area that opposed its net change in burned area (Tables 2, 3). Of the five ecoregions that experienced the greatest net change in burned area from the 1980s to the 2010s, three (Northeastern Siberian Taiga, Northern Canadian Shield Taiga, and Canadian Aspen Forests and Parkland Forests) also experienced significant increasing trends in annual burned area. Of those ecoregions that experienced a negative net change in burned area from the 1980s to the 2010s, only one (Eastern Canadian Shield Taiga) also experienced a significant decreasing trend in annual burned area. Across the circumboreal region, the Northeast Siberian Taiga ecoregion

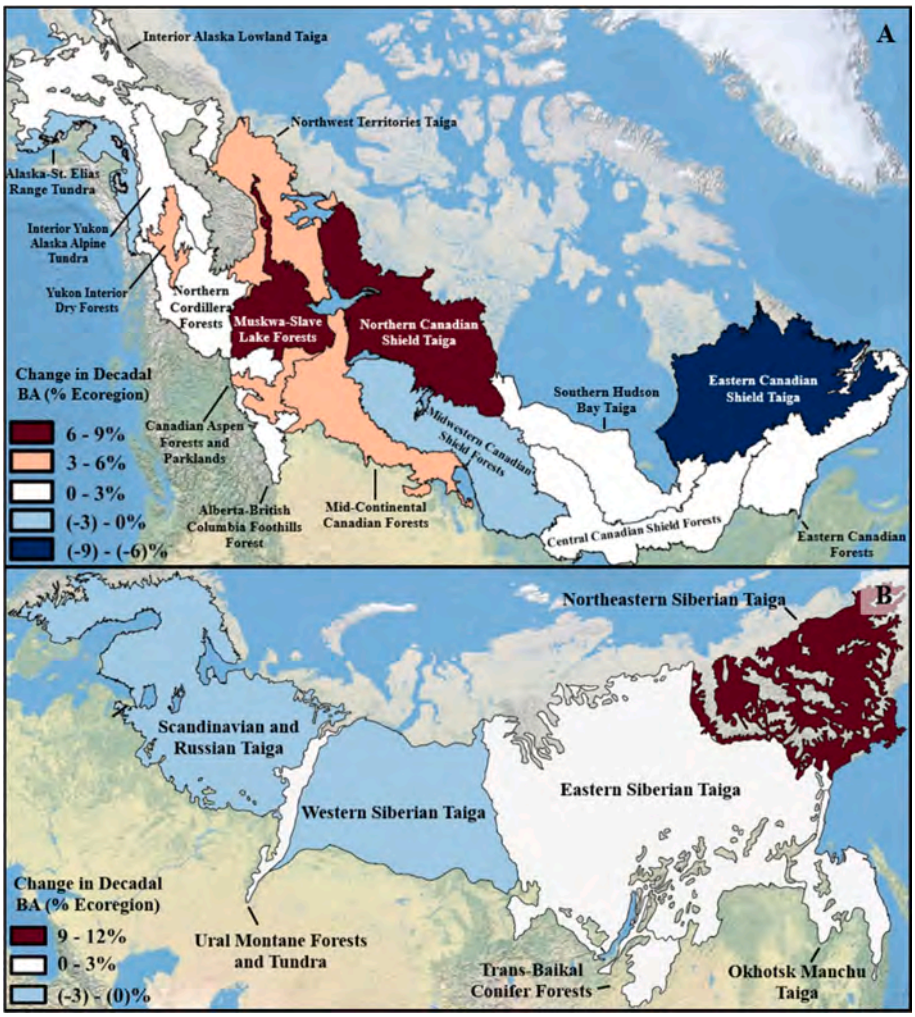

Fig. 7. Net difference in total North American (A) and Eurasian (B) ecoregion level boreal forest burned area occurring between the years of 1983–1992 and 2011–2020 expressed as a percentage point change in ecoregion area. Thirteen North American and five Eurasian boreal ecoregions experienced a greater amount of burning between 2011 and 2020 than they did between 1983 and 1992. Overall, 1.69 % and 3.49 % more of boreal forests burned within North America and Eurasia between 2011 and 2020 than between 1983 and 1992.

experienced both the greatest increasing trend and third greatest change in annual burned area between the 1980s and 2010s (1.37 %yr^{-1}, p = 0.13 and 231.6 % net change), while the Eastern Canadian Shield Taiga experienced the greatest decreasing trend and change in annual burned area (−0.56 %yr^{-1}, p = 0.06 and − 63.1 % net change).

3.5. Comparison of Burned Area Trends with MTBS, NRC, MCD64A1v61, and FireCCILT11 Burned Area Time Series

Comparison of our AVHRR and MODIS-based burned area datasets with reference burned area datasets showed general agreement in observed trends at the continental scale (Table 3). Across North American boreal forests, we found non-significant increases in burned area of 0.19 %yr^{-1} (p = 0.24) and 0.15 %yr^{-1} (p = 0.37) across our 37-year AVHRR dataset and the 36-year MTBS/NRC reference dataset when only overlapping years of observation were examined (1984–2020, no 1994). Comparison of our 20-year AVHRR, MODIS-BAI, and MODIS-NBR burned area datasets with the 20-year MTBS/NRC and MCD64A1v61 reference burned area dataset found similar results. Whereas our 20-year AVHRR dataset showing a significant (p = 0.09) decreasing trend of −0.59 %yr^{-1}, the MODIS-BAI, MODIS-NBR, MCD64A1v61, and 20-year MTBS/NRC datasets showed non-significant decreases in burning of −0.02 %yr^{-1}, −0.05 %yr^{-1}, −0.35 %yr^{-1}, and − 0.31 %yr^{-1} respectively. For Eurasia, we found that burned area significantly increased by 0.56 %yr^{-1} (p = 0.09) across our 37-year AVHRR dataset. In contrast, we found a non-significant decrease in burned area of −0.39 %yr^{-1} across our 20-year AVHRR dataset, and non-significant increases in burning of 1.31 %yr^{-1}, 1.14 %yr^{-1}, and 0.17 %yr^{-1} across our MODIS BAI, NBR, and the MCD64A1v61 burned area datasets respectively.

We also found general agreement in burned area trends observed among North American boreal ecoregions between our 37-year AVHRR dataset and the 36-year MTBS/NRC reference burned area dataset when evaluated over shared years of observation. Burned area significantly (α = 0.1) increased across our 37-year AVHRR dataset within the Northern Cordillera Forests (0.15 %yr^{-1}), Northern Canadian Shield Taiga (0.70 %yr^{-1}), Interior Alaska Yukon Lowland Taiga (0.97 %yr^{-1}), and Canadian Aspen Forests and Parkland Forests (0.17 %yr^{-1}) ecoregions. Likewise, burned area also significantly increased by 0.39 %yr^{-1} within the Northern Cordillera Forests ecoregion, and was suggested to have increased in the Northern Canadian Shield Taiga (0.74 %yr^{-1}, p = 0.13), Interior Alaska Yukon Lowland Taiga (0.89 %yr^{-1}, p = 0.17), and Canadian Aspen Forests and Parkland Forests (0.17 %yr^{-1}, p = 0.16) ecoregions across the MTBS/NRC reference dataset over this timespan. Finally, we found that burned area significantly decreased within the Eastern Canadian Shield Taiga ecoregion by (0.17 %yr^{-1}, p = 0.03) across our 37-year AVHRR dataset and was suggested to have (−0.58 % yr^{-1}, p = 0.11) across the 36-year MTBS/NRC reference dataset. The

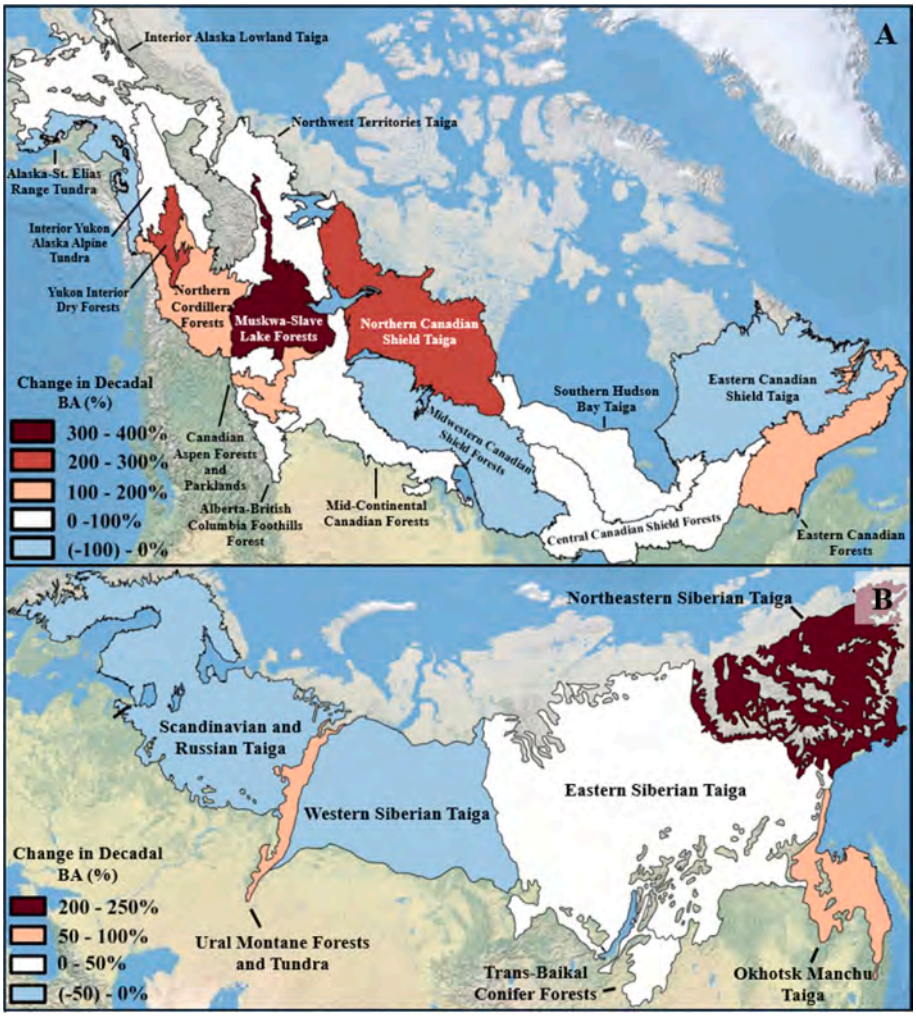

Fig. 8. Change in total North American (A) and Eurasian (B) ecoregion level boreal forest burned area occurring between the years of 1983–1992 and 2011–2020 expressed as percentage increase in burned area. Overall burned area increased proportionally by 0.48, 0.54, and 0.53 across the North American, Eurasian, and Circumboreal region, respectively.

omission of 1994, the third largest fire year within the MTBS/NRC reference dataset (1984–2020), due to the AVHRR data gap (Dech et al., 2021) may bias analyses (Oton et al., 2021b). To evaluate whether this data gap influenced results, we compared trends in the MTBS/NRC reference dataset when including and excluding 1994. We found no change in the significance of observed trends in any ecoregion or the continent (Table 3, Table S7).

We found similar agreement between our burned area datasets and reference burned area products within Eurasian boreal ecoregions. The significant ($\alpha = 0.1$) increase in burned area observed within the East Siberian Taiga ecoregion across our MODIS BAI (4.31 $\%yr^{-1}$, $p = 0.08$) and NBR (5.71 $\%yr^{-1}$, $p = 0.03$) time series was also present in the MCD64A1v61 (4.59 $\%yr^{-1}$, $p = 0.03$) time series, though not significant across our 20-year AVHRR time series (3.70 $\%yr^{-1}$, $p = 0.29$). Finally, the significant decrease in annual burned area within the Scandinavian and Russian Taiga ecoregion observed across our 20-year AVHRR (-2.76 $\%yr^{-1}$, $p = 0.04$), MODIS BAI (-0.49 $\%yr^{-1}$, $p = 0.01$) and NBR (-0.29 $\%yr^{-1}$, $p = 0.07$) time series was also present in the MCD64A1v61 (-1.30 $\%yr^{-1}$, $p = 0.01$) time series.

When we compared trends in burned area between our AVHRR-based burned area dataset and the AVHRR-based FireCCILT11 across overlapping years of data (1983–2018, no 1994) we found rather inconsistent results (Table S7). For the two continents, our AVHRR-based burned area dataset showed a significant increase in annual burned area across the North American continental region (0.33 $\%yr^{-1}$, $p = 0.05$), which was not present in the FireCCILT11 dataset. However, the FireCCILT11 showed a significant decrease in annual burned area across the Eurasian continental region (-0.35 $\%yr^{-1}$, $p = 0.09$), which was not present in our AVHRR-based burned area dataset. At the ecoregion level, our AVHRR-based burned area dataset showed significant increases in seven ecoregions across the global circumboreal region. Among those seven, only the trends within the Interior Alaska Yukon Lowland Taiga and Northern Canadian Shield Taiga were also present within the FireCCILT11 dataset. However, the FireCCILT11 dataset showed significant trends within four ecoregions that were not present in our AVHRR-based burned area dataset. Potential explanations for these disagreements in burned area trends are the influence of SZA on the FireCCILT11 dataset (Giglio and Roy, 2022), and artifacts caused by the FireCCILT11's method of subpixel burned area estimate (Giglio and Roy, 2023) which potentially afflict the pre-MODIS era (⟨2001) (Supplment 8) through omission of large fires (Supplement 9).

4. Discussion

Tracking long-term change in circumboreal burned area is challenging because Landsat data are sparse in Eurasia prior to 2000, and the AVHRR LTDR archive is the only remote sensing dataset available for Eurasia for the 1980s and '90s (Berner et al., 2020; Berner and Goetz,

Table 3
Circumboreal annual burned area trends for AVHRR and MODIS derived burned area datasets expressed as % per year (%yr^{-1}). Overlapping years (1984–2020, no 1994) of AVHRR and MTBS/NRC Landsat observations are reported as "paired" time series.

Ecoregion	AVHRR BAI (1983–2020)		MTBS/NRC (Paired)		AVHRR BAI (Paired)		AVHRR BAI (2001–2020)		MODIS BAI (2001–2020)		MODIS NBR (2001–2020)		MCD64A1v61 (2001–2020)		MTBS/NRC (2001–2020)	
Bold: Significant (α = 0.1)	Trend	Sig.	Trend	Sig.	Trend	Sig.	Trend	Sig.	Trend	Sig.	Trend	Sig.	Trend	Sig.	Trend	Sig.
Alaska St Elias Range Tundra	−0.07	0.45	0.03	0.52	−0.09	0.44	−0.21	0.49	−0.02	0.79	−0.02	0.82	0.02	0.81	0.01	0.94
Alberta British Columbia Foothills	**0.12**	**0.09**	0.09	0.28	0.11	0.13	**0.29**	**0**	**0.15**	**0.05**	**0.28**	**0**	0.14	0.13	**0.24**	**0.03**
Canadian Aspen Forests and Parklands Forests	**0.17**	**0.02**	0.17	0.16	**0.17**	**0.02**	**0.34**	**0.03**	0.16	0.34	**0.38**	**0.03**	**0.58**	**0.03**	**0.60**	**0.04**
Central Canadian Shield Forests	−0.25	0.23	−0.24	0.43	−0.25	0.25	**−0.86**	**0.03**	−0.16	0.67	−0.40	0.31	**−0.77**	**0.06**	**−0.72**	**0.05**
Eastern Canadian Forests	0.23	0.24	0.13	0.55	0.21	0.29	−0.36	0.52	0.06	0.92	−0.28	0.63	−0.63	0.28	−0.73	0.20
Eastern Canadian Shield Taiga	**−0.56**	**0.06**	−0.58	0.11	**−0.64**	**0.03**	**−0.86**	**0.04**	−0.02	0.96	−0.27	0.49	**−0.86**	**0.04**	−0.73	0.12
Interior Alaska Yukon Lowland Taiga	**1.07**	**0.07**	0.89	0.17	**0.97**	**0.10**	−0.20	0.92	−1.21	0.24	−0.62	0.62	−1.40	0.36	−1.45	0.33
Interior Yukon Alaska Alpine Tundra	0.22	0.57	0.11	0.78	0.18	0.66	−1.13	0.35	−0.80	0.23	−1.14	0.25	−1.28	0.18	−1.49	0.18
Mid Continental Canadian Forests	**0.44**	**0.1**	**0.67**	**0.01**	0.36	0.17	−0.66	0.19	0.71	0.25	0.74	0.22	0.80	0.28	0.92	0.26
Midwestern Canadian Shield Forests	0.31	0.35	0.49	0.35	0.28	0.41	**−1.50**	**0**	−0.21	0.81	−0.21	0.81	−0.80	0.34	−0.60	0.46
Muskwa Slave Lake Forests	0.18	0.72	0.56	0.24	0.10	0.85	−0.85	0.28	−0.05	0.94	0.16	0.85	0.33	0.77	0.57	0.63
Northern Canadian Shield Taiga	**0.78**	**0.05**	0.74	0.13	**0.70**	**0.09**	0.30	0.76	1.22	0.22	0.77	0.48	0.68	0.46	0.64	0.59
Northern Cordillera Forests	**0.13**	**0.04**	**0.39**	**0.01**	**0.15**	**0.03**	−0.04	0.8	0.21	0.3	0.24	0.22	−0.07	0.79	0.33	0.23
Northwest Territories Taiga	−0.10	0.77	−0.32	0.45	−0.21	0.52	0.38	0.42	0.77	0.25	0.82	0.27	0.89	0.29	0.91	0.37
Southern Hudson Bay Taiga	0.04	0.84	−0.15	0.50	0.02	0.90	**−0.95**	**0.04**	−0.14	0.7	−0.24	0.54	−0.54	0.28	−0.57	0.27
Yukon Interior Dry Forests	−0.01	0.98	0.02	0.86	−0.01	0.92	−0.05	0.63	−0.09	0.42	−0.02	0.91	0.01	0.97	0.02	0.90
East Siberian Taiga	1.36	0.24	–	–	–	–	3.70	0.29	**4.31**	**0.08**	**5.71**	**0.03**	**4.59**	**0.03**	**–**	**–**
Northeast Siberian Taiga	**1.37**	**0.13**	–	–	–	–	−0.35	0.93	3.28	0.38	2.53	0.42	1.51	0.70	–	–
Okhotsk Manchu Taiga	0.27	0.47	–	–	–	–	−0.44	0.30	0.38	0.32	0.01	0.98	−0.78	0.30	–	–
Scandinavian and Russian Taiga	−0.05	0.93	–	–	**–**	**–**	**−2.76**	**0.04**	**−0.49**	**0.01**	**−0.29**	**0.07**	**−1.30**	**0.01**	**–**	**–**
Trans Baikal Conifer Forests	−0.02	0.97	–	–	–	–	−1.30	0.11	−0.65	0.26	**−1.05**	**0.06**	−1.45	0.15	–	–
Ural Montane Forests and Tundra	0.06	0.47	–	–	–	–	−0.21	0.34	−0.04	0.48	−0.07	0.36	−0.06	0.41	–	–
Western Siberian Taiga	0.12	0.81	–	–	–	–	−0.43	0.78	0.93	0.38	**0.57**	**0.08**	−1.10	0.51	–	–
Entire North American Boreal Region	0.24	0.12	0.15	0.37	0.19	0.24	**−0.59**	**0.09**	−0.02	0.95	−0.05	0.86	−0.35	0.35	−0.31	0.41
Entire Eurasian Boreal Region	**0.56**	**0.10**	–	–	–	–	−0.39	0.72	1.31	0.44	1.14	0.32	0.17	0.86	–	–

2022; Garcia-Lazaro et al., 2018). However, limitations of the AVHRR LTDR archive (Dech et al., 2021) complicate its use for burned area mapping (Giglio and Roy, 2020; Giglio and Roy, 2022). Our new time-series analysis based burned area mapping method successfully addressed the major limitations of the AVHRR dataset, and provided accurate and consistent annual burned area maps starting in 1983 for the circumboreal region. However, our method's focus on mapping large wildfires suggests that the influence of smaller, less severe wildfires on annual burned area estimates and observed trends may be under-estimated. This bias likely has the greatest impact on estimates of burning in Eurasian boreal forests where 30–50 % of fires are less than 200 ha in size (de Groot et al., 2013), and our AVHRR-based burned area dataset had the lowest agreement with higher-resolution validation datasets (Table 1). Finally, our method requires that burned areas are visible for several years, and that probably limits the applicability of our method in regions with smaller fires and where vegetation recovery is rapid, such as grasslands (Wang et al., 2022; Morgan et al., 2014).

Our 37-year AVHRR burned area dataset found a mildly significant ($p = 0.10$) increasing trend in boreal forest annual burned area at the Eurasian continental-scale and a suggested ($p = 0.12$) increasing burned area trend at the North American continental-scale. At the ecoregion scale, we found that annual burned area likely increased between the years of 1983 and 2020 across seven ecoregions, which account for 19.6 % of circumboreal forests (35 % of North American and 11 % of Eurasian boreal forests). These ecoregions alone equal approximately the size of India. These trends agree with the observed net change in total inter-decadal burned area, with no ecoregion exhibiting a significant annual burned area trend conflicting with its coincident interdecadal change in burned area.

Finally, when we compared our 37-year AVHRR burned area dataset to the MCD64A1v61 reference burned area dataset, we found that one out of the two significant increasing burned area trends detected in the MCD64A1v61 burned area dataset were also present within our 37-year AVHRR burned area dataset. This agreement in results suggests that observed increases in burned area are not an artifact of the MCD64A1v61 archive's shorter time series (Mouillot et al., 2014) and indeed represent ongoing change experienced by this landscape. Conversely, the omission of increasing burned area trend observed within the Interior Alaska Lowland Taiga, Mid Continental Canadian Forests, Northern Canadian Shield Taiga, and Northern Cordillera Forest

Fig. 9. Trends in burned area expressed as percent per year (%yr^{-1}) within North American (A) and Eurasian (B) boreal forests estimated across our AVHRR-derived (1983–2020) burned area dataset. Only trends observed in the Alberta British Columbia Foothills, Canadian Aspen Forests and Parklands Forests, Eastern Canadian Shield Taiga, Interior Alaska Yukon Lowland Taiga, Mid Continental Canadian Forests, Northern Canadian Shield Taiga, Northern Cordillera Forests ecoregions are statistically significant ($p < 0.1$). However, the trend observed within the Northeastern Siberian Taiga ecoregion is suggested (p = 0.13).

ecoregions across our 37-year AVHRR burned area dataset by both the MCD64A1v61 archive and our 20-year AVHRR dataset highlights the challenge of detecting long-term change in burned area using short time series. This challenge is particularly salient when studying boreal fire regimes, which exhibit large interannual variability (Jain et al., 2017, Tomshin and Solovyev) and have fire return intervals ranging from decades to centuries (Baltzer et al., 2021; Burrell et al., 2022). Addressing this challenge is an important contribution of our 37-year AHVRR time series.

4.1. Comparison with existing studies on circumboreal burned area

One reason why circumboreal burned area changes and trends are important is because they may be caused by climate change (IPCC, 2021) (Bedia et al., 2015; Forkel et al., 2019). The availability of a multi-decadal Landsat and high-quality federal fire management datasets have enabled extensive study of North American boreal burned area trends (Kasischke and Turetsky, 2006; Veraverbeke et al., 2017; Hanes et al., 2019). However, no similar multidecadal resources exist for Eurasian boreal forests (Conard et al., 2002; Chen et al., 2014) necessitating the use of coarse resolution (Garcia-Lazaro et al., 2018) or short-time series datasets (Talucci et al., 2022; Tian et al., 2022). Analyses of multi-decadal North American boreal forest burned area extent have identified increases, but no significant trends in burned area (Jones et al., 2022). These results agree with the continental-scale analyses of our 37-year AVHRR burned area dataset and the 36-year MTBS/NRC reference dataset which reported nonsignificant increases in burning of 0.15 % yr^{-1} ($p = 0.37$) and (0.19 %yr^{-1}, $p = 0.24$) in annual burned area across shared years of observation, respectively.

At regional scales, multi-decadal studies have found non-significant increases in annual Alaskan forest burned area (Veraverbeke et al., 2017; Jones et al., 2022). These results again partially agree with our results for the three corresponding Alaskan ecoregions with two ecoregions (Alaska St. Elias Range Tundra and Interior Yukon Alaska Alpine Tundra) exhibiting non-significant increase according to both our 37-year AVHRR dataset ($p > 0.4$) and the MTBS/NRC reference dataset ($p > 0.5$). However, our results differ for the Interior Alaska Yukon Lowland Taiga ecoregion with our 37-year AVHRR dataset showing a mildly significant (0.97 %yr^{-1}, $p = 0.10$) increasing trend and the MTBS/NRC reference dataset suggesting (0.89 %yr^{-1}, $p = 0.17$) an increasing trend in annual burned area across shared years of observations. Documented multi-decadal burned area trends across Canadian boreal forests are more heterogenous than those observed in Alaska (Jones et al., 2022). Regional increases in burned area have occurred within western Canadian forests (Coops et al., 2018; Hanes et al., 2019). Interestingly, across the six ecoregions spanning western Canadian boreal forests, only three (Northern Cordillera Forests, Mid Continental Canadian Forests, and Canadian Aspen Forests and Parkland Forests)

exhibit or suggest increasing trends in both our 37-year AVHRR (0.15 % yr^{-1} $p = 0.03$, 0.36 %yr^{-1} $p = 0.17$, and 0.17 %yr^{-1} $p = 0.02$, respectively) and MTBS/NRC reference dataset (0.39 %yr^{-1} $p = 0.01$, 0.67 % yr^{-1} $p = 0.01$, and 0.17 %yr^{-1} $p = 0.16$, respectively) across shared years of observations.

The sparsity of pre-2000 Landsat images has impeded study of Eurasian boreal forest burned area (Shvidenko et al., 2011; Berner et al., 2012; Ponomarev et al., 2016) and resulted in conflicting statements about trends (Tian et al., 2022). Analyses of Eurasian boreal forest burned area using short (<20 year) time series have reported non-significant increases in burned area at the continental scale (Soja et al., 2007; Krylov et al., 2014; Kukavskaya et al., 2016). These findings partially agree with continental scale analysis of our 37-year AVHRR burned area dataset which showed a mildly significant ($p = 0.1$) increasing trend in annual burned area 0.56 %yr^{-1}. At the regional scale, decreasing trends in burned area have been observed over the MODIS era (2001–2020) in western Siberia (Tomshin and Solovyev, 2021), while increasing multi-decadal increasing trends have been observed in Eastern Siberia (Garcia-Lazaro et al., 2018).

Analysis of our MODIS and 37-year AVHRR burned area datasets within the two corresponding ecoregions shows mixed agreement with these findings. While we found suggested increasing burned area trends across our AVHRR 37-year burned area dataset within the Northeastern Siberian Taiga ecoregion (1.36 %yr^{-1}, $p = 0.13$), only our 20-year AVHRR, MODIS-BAI, and MODIS-NBR based datasets show significant decreasing trends in burned area within the Scandinavian and Russian Taiga ecoregion (−2.76 %yr^{-1} $p = 0.04$, −0.49 %yr^{-1}, $p = 0.01$, and −0.29 %yr^{-1} $p = 0.07$, respectively). A potential explanation for this discrepancy could be that short-term declining trends in burned area are overridden by multidecadal (1983–2020) time series. Another reason for differences in our results from those previously reported is that all referenced studies on burned area trends employ either the Mann-Kendall test with Theil-Sen slope estimator or simple linear regression time series analysis to test for annual burned area trends. These methods do not account for temporal autocorrelation in time series values and therefore are susceptible to time-trend commission errors due to non-independence in observations (Ives et al., 2021). Therefore, the statistical significance of those reported trends should be viewed with caution.

4.2. Influence of solar zenith angle on AVHRR burned area dataset

Comparison of our AVHRR burned area datasets including and excluding SZA as BAI time series model covariates found that exclusion of SZA erroneously increased mapped burned area during high-SZA years (Supplement 5). Supporting this, we found that this difference in annual mapped burned area was positively correlated ($p < 0.01$) with annual average SZA of observation, and that this relationship accounted for 19 % and 33 % of variation in this difference for North American and Eurasian burned area datasets, respectively. These results suggest that burned area mapping accuracy can be substantially reduced due to commission errors during high SZA years. Moreover, these results also show that inclusion of SZA's polynomial relationship with 90th percentile BAI as time series model covariates reduces but does not eliminate the influence of trends in SZA on burned area mapping accuracy. However, errors in burned area mapping during high-SZA years may result from coexisting drivers such as progressive sensor degradation near sensor end of life (Ji and Brown, 2017) and thus represents a limitation of the AVHRR LTDR archive itself (Key et al., 2019b).

5. Conclusion

We successfully developed and applied a burned area mapping algorithm based on statistical time-series analysis which accounts for the effects of solar zenith angle of observation and sensor-based biases on AVHRR data. We used this algorithm to map annual circumboreal burned area with AVHRR data between the years of 1983 and 2020, and used these maps to both quantify decadal change and test for long term trends in burned area. We found that circumboreal burned area increased proportionally by 0.53 in the 2010s compared to the 1980s, and that burned area had at least doubled in seven boreal ecoregions over this period. Moreover, we found increasing, mildly significant multidecadal (1983–2020) trends in annual burned area extent across Eurasian boreal forests and suggested increasing burned area trends across North American boreal forests. At the regional scale, we found seven ecoregions comprising a region approximately the size of India to have experienced significant increases in annual burned area over the last four decades. Our results broadly agree with those found using the 20-year (2001–2020) MCD64A1v61 archive, with most ecoregion-level increasing burned area trends identified in the MCD64A1v61 archive also present within our multidecadal AVHRR burned area time series.

However, burned area trends estimated with both the MCD64A1v61 archive and our 20-year AVHRR burned area dataset did not detect the increasing burned area trends which we observed in four ecoregions using our 37-year AVHRR burned area dataset. This highlights the challenge of detecting burned area trends in boreal fire regimes with shorter times series because of longer fire return intervals, and why AVHRR-based burned area mapping, despite the limitations of the sensor and dataset is valuable and informative.

CRediT authorship contribution statement

Connor W. Stephens: Writing – review & editing, Writing – original draft, Validation, Methodology, Investigation, Funding acquisition, Formal analysis, Data curation, Conceptualization. **Anthony R. Ives:** Writing – review & editing, Methodology, Investigation, Formal analysis. **Volker C. Radeloff:** Writing – review & editing, Supervision, Methodology, Investigation, Funding acquisition, Conceptualization.

Declaration of competing interest

All authors declare that they have no known competing financial interests or personal relationships that could have appeared to influence their work.

Data availability

All burned area datasets created in this analysis are available for download on the SILVIS Lab website at https://geoserver.silvis.forest.wisc.edu/geodata/boreal-burned-area/.

Acknowledgements

We thank the National Aeronautics and Space Administration (NASA) Advanced Information Systems Technology, Interdisciplinary Science, and Future Investigators in NASA Earth and Space Science and Technology programs for providing funding for this research. Additionally, we thank Dr. T. L'Ecuyer, Dr. M. Ozdogan, and Dr. C. Andresen for their guidance in subject formulation and methodological development. We also appreciate the input from Dr. C. Morrow and Dr. J. Botsch on statistical time series analysis. Finally, we thank K. Pfoch and H. Cox for comments on earlier versions of this manuscript.

Appendix A. Supplementary data

Supplementary data to this article can be found online at https://doi.org/10.1016/j.rse.2025.114789.

References

Astrup, R., Bernier, P., Genet, H., Lutz, D., Bright, R., 2018. A sensible climate solution for the boreal forest. Nat. Clim. Chang. 8, 11–12.

Baltzer, J.L., Day, N.J., Walker, X.J., Greene, D., Mack, M.C., Alexander, H.D., Arseneault, D., Barnes, J., Bergeron, Y., Boucher, Y., Bourgeau-Chavez, L., Brown, C. D., Carriere, S., Howard, B.K., Gauthier, S., Parisien, M.A., Reid, K.A., Rogers, B.M., Roland, C., Sirois, L., Stehn, S., Thompson, D.K., Turetsky, M.R., Veraverbeke, S., Whitman, E., Yang, J., Johnstone, J.F., 2021. Increasing fire and the decline of fire adapted black spruce in the boreal forest. Proc. Natl. Acad. Sci. USA 118.
Barrett, K., Baxter, R., Kukavskaya, E., Balzter, H., Shvetsov, E., Buryak, L., 2020. Postfire recruitment failure in scots pine forests of southern Siberia. Remote Sens. Environ. 237.
Baumann, M., Ozdogan, M., Wolter, P.T., Krylov, A., Vladimirova, N., Radeloff, V.C., 2014. Landsat remote sensing of forest windfall disturbance. Remote Sens. Environ. 143, 171–179.
Bedia, J., Herrera, S., Gutierrez, J.M., Benali, A., Brands, S., Mota, B., Moreno, J.M., 2015. Global patterns in the sensitivity of burned area to fire-weather: implications for climate change. Agric. For. Meteorol. 214, 369–379.
Berner, L.T., Goetz, S.J., 2022. Satellite observations document trends consistent with a boreal forest biome shift. Glob. Chang. Biol. 28, 3275–3292.
Berner, L.T., Beck, P.S.A., Loranty, M.M., Alexander, H.D., Mack, M.C., Goetz, S.J., 2012. Cajander larch (Larix cajanderi) biomass distribution, fire regime and post-fire recovery in northeastern Siberia. Biogeosciences 9, 3943–3959.
Berner, L.T., Massey, R., Jantz, P., Forbes, B.C., Macias-Fauria, M., Myers-Smith, I., Kumpula, T., Gauthier, G., Andreu-Hayles, L., Gaglioti, B.V., Burns, P., Zetterberg, P., D'Arrigo, R., Goetz, S.J., 2020. Summer warming explains widespread but not uniform greening in the Arctic tundra biome. Nat. Commun. 11.
Bond-Lamberty, B., Peckham, S.D., Ahl, D.E., Gower, S.T., 2007. Fire as the dominant driver of Central Canadian boreal forest carbon balance. Nature 450, 89–+.
Bonsal, B.R., Cuell, C., Wheaton, E., Sauchyn, D.J., Barrow, E., 2017. An assessment of historical and projected future hydro-climatic variability and extremes over southern watersheds in the Canadian prairies. Int. J. Climatol. 37, 3934–3948.
Bosch, M., Ives, A., 2023. Identifying environmental factors affecting the production of pea aphid dispersal morphs in field populations. Ecolog. Entol. 48, 597–609.
Boschetti, L., Flasse, S., Brivio, P., 2004. Analysis of the conflict between omission and commission in low spatial resolution dichotomic thematic products: the Pareto boundary. Remote Sens. Environ. 91, 280–292.
Boschetti, L., Roy, D.P., Giglio, L., Huang, H.Y., Zubkova, M., Humber, M.L., 2019. Global validation of the collection 6 MODIS burned area product. Remote Sens. Environ. 235.
Bowman, D., Kolden, C.A., Abatzoglou, J.T., Johnston, F.H., van der Werf, G.R., Flannigan, M., 2020. Vegetation fires in the Anthropocene. Nat. Rev. Earth & Environment 1, 500–515.
Box, G.E., Jenkins, G.M., Reinsel, G.C., 1994. Time Series Analysis: Forecasting and Control, 3rd edition. Prentice Hall, Englewood Cliffs, New Jersey USA.
Bradshaw, C.J.A., Warkentin, I.G., 2015. Global estimates of boreal forest carbon stocks and flux. Glob. Planet. Chang. 128, 24–30.
Burrell, A.L., Sun, Q.Q., Baxter, R., Kukavskaya, E.A., Zhila, S., Shestakova, T., Rogers, B. M., Kaduk, J., Barrett, K., 2022. Climate change, fire return intervals and the growing risk of permanent forest loss in boreal Eurasia. Sci. Total Environ. 831.
Chander, G., Xiong, X.X., Choi, T.Y., Angal, A., 2010. Monitoring on-orbit calibration stability of the Terra MODIS and Landsat 7 ETM+ sensors using pseudo-invariant test sites. Remote Sens. Environ. 114, 925–939.
Chen, D., Loboda, T., Channan, S., Hoffman-Hall, A., 2014. Long-term record of sampled disturbances in northern Eurasian boreal Forest from Pre-2000 Landsat data. Remote Sens. 6, 6020–6038.
Chuvieco, E., Martin, M.P., Palacios, A., 2002. Assessment of different spectral indices in the red-near-infrared spectral domain for burned land discrimination. Int. J. Remote Sens. 23, 5103–5110.
Conard, S.G., Sukhinin, A.I., Stocks, B.J., Cahoon, D.R., Davidenko, E.P., Ivanova, G.A., 2002. Determining effects of area burned and fire severity on carbon cycling and emissions in Siberia. Clim. Chang. 55, 197–211.
Coops, N.C., Hermosilla, T., Wulder, M.A., White, J.C., Bolton, D.K., 2018. A thirty year, fine-scale, characterization of area burned in Canadian forests shows evidence of regionally increasing trends in the last decade. PLoS One 13.
Cortes, J., Mahecha, M.D., Reichstein, M., Myneni, R.B., Chen, C., Brenning, A., 2021. Where are global vegetation greening and Browning trends significant? Geophys. Res. Lett. 48.
de Groot, W.J., Cantin, A.S., Flannigan, M.D., Soja, A.J., Gowman, L.M., Newbery, A., 2013. A comparison of Canadian and Russian boreal forest fire regimes. For. Ecol. Manag. 294, 23–34.
Dech, S., Holzwarth, S., Asam, S., Andresen, T., Bachmann, M., Boettcher, M., Dietz, A., Eisfelder, C., Frey, C., Gesell, G., Gessner, U., Hirner, A., Hofmann, M., Kirches, G., Klein, D., Klein, I., Kraus, T., Krause, D., Plank, S., Popp, T., Reinermann, S., Reiners, P., Roessler, S., Ruppert, T., Scherbachenko, A., Vignesh, R., Wolfmueller, M., Zwenzner, H., Kuenzer, C., 2021. Potential and challenges of harmonizing 40 years of AVHRR data: the TIMELINE experience. Remote Sens. 13.
Descals, A., Gaveau, D., Verger, A., Sheil, D., Naito, D., Peñuelas, J., 2022. Unprecedented fire activity above the Arctic circle linked to rising temperatures. SCIENCE 378, 532–537.
Didan, K., 2015. MOD13Q1 MODIS/Terra Vegetation Indices 16-Day L3 Global 250m SIN Grid V006 (NASA EOSDIS Land Processes DAAC).
Dieleman, C.M., Rogers, B.M., Potter, S., Veraverbeke, S., Johnstone, J.F., Laflamme, J., Solvik, K., Walker, X.J., Mack, M.C., Turetsky, M.R., 2020. Wildfire combustion and carbon stocks in the southern Canadian boreal forest: implications for a warming world. Glob. Chang. Biol. 26, 6062–6079.
Fensholt, R., Proud, S.R., 2012. Evaluation of Earth observation based global long term vegetation trends - comparing GIMMS and MODIS global NDVI time series. Remote Sens. Environ. 119, 131–147.
Forkel, M., Dorigo, W., Lasslop, G., Chuvieco, E., Hantson, S., Heil, A., Teubner, I., Thonicke, K., Harrison, S.P., 2019. Recent global and regional trends in burned area and their compensating environmental controls. Environ. Res. Communicat. 1.
Franch, B., Vermote, E.F., Roger, J.C., Murphy, E., Becker-Reshef, I., Justice, C., Claverie, M., Nagol, J., Csiszar, I., Meyer, D., Baret, F., Masuoka, E., Wolfe, R., Devadiga, S., 2017. A 30+year AVHRR land surface reflectance climate data record and its application to wheat yield monitoring. Remote Sens. 9.
Garcia-Lazaro, J.R., Moreno-Ruiz, J.A., Riano, D., Arbelo, M., 2018. Estimation of burned area in the northeastern Siberian boreal Forest from a long-term data record (LTDR) 1982-2015 time series. Remote Sens. 10.
Gauthier, S., Bernier, P., Kuuluvainen, T., Shvidenko, A.Z., Schepaschenko, D.G., 2015. Boreal forest health and global change. Science 349, 819–822.
Giglio, L., Roy, D.P., 2020. On the Outstanding Need for a Long-Term, Multi-Decadal, Validated and Quality Assessed Record of Global Burned Area: Caution in the Use of Advanced Very High Resolution Radiometer Data. Science of Remote Sensing. Elsevier.
Giglio, L., Roy, D., 2022. Assessment of Satellite Orbit-Drift Artifacts in the Long-Term AVHRR FireCCILT11 Global Burned Area Data Set. 100044. Science of Remote Sensing: Elsevier.
Giglio, L., Roy, D., 2023. FireCCILT11 artifacts may confound the link between biomass burning and infant mortality. In: PROCEEDINGS OF THE NATIONAL ACADEMY OF SCIENCES OF THE UNITED STATES OF AMERICA, p. 120.
Giglio, L., Justice, C., Boschetti, L., Roy, D., 2015. MCD64A1 MODIS/Terra+Aqua Burned Area Monthly L3 Global 500m SIN Grid V006 Burnt Area Product (NASA EOSDIS Land Processes DAAC).
Giglio, L., Boschetti, L., Roy, D.P., Humber, M.L., Justice, C.O., 2018. The collection 6 MODIS burned area mapping algorithm and product. Remote Sens. Environ. 217, 72–85.
Giglio, L., Zubkova, M., Roy, D.P., 2022. Comment on Oton et al. Analysis of Trends in the FireCCI Global Long Term Burned Area Product (1982-2018). Fire 4, 74. Fire-Switzerland, 5.
Grillakis, M., Voulgarakis, A., Rovithakis, A., Seiradakis, K.D., Koutroulis, A., Field, R.D., Kasoar, M., Papadopoulos, A., Lazaridis, M., 2022. Climate drivers of global wildfire burned area. Environ. Res. Lett. 17.
Guo, R., Yan, J., Zheng, H., Wu, B., 2024. Assessment of the Analytic Burned Area Index for Forest Fire Severity Detection Using Sentinel and Landsat Data (FIRE-SWITZERLAND).
Hanes, C.C., Wang, X.L., Jain, P., Parisien, M.A., Little, J.M., Flannigan, M.D., 2019. Fire-regime changes in Canada over the last half century. Can. J. For. Res. 49, 256–269.
Holloway, J.E., Lewkowicz, A.G., Douglas, T.A., Li, X.Y., Turetsky, M.R., Baltzer, J.L., Jin, H.J., 2020. Impact of wildfire on permafrost landscapes: a review of recent advances and future prospects. Permafr. Periglac. Process. 31, 371–382.
IPCC, 2021. Climate Change2021: They Physical Science Basis. Cambridge University Press.
Ives, A.R., Helmus, M.R., 2011. Generalized linear mixed models for phylogenetic analyses of community structure. Ecol. Monogr. 81, 511–525.
Ives, A., Zhu, L., Wang, F., Zhu, J., Morrow, C., Radeloff, V., 2021. Statistical inference for spatiotemporal trends in remote-sensing data. Remote Sens. 266, 112679.
Jain, P., Wang, X.L., Flannigan, M.D., 2017. Trend analysis of fire season length and extreme fire weather in North America between 1979 and 2015. Int. J. Wildland Fire 26, 1009–1020.
Ji, L., Brown, J.F., 2017. Effect of NOAA satellite orbital drift on AVHRR-derived phenological metrics. Int. J. Appl. Earth Obs. Geoinf. 62, 215–223.
Jones, M.W., Abatzoglou, J.T., Veraverbeke, S., Andela, N., Lasslop, G., Forkel, M., Smith, A.J.P., Burton, C., Betts, R.A., van der Werf, G.R., Sitch, S., Canadell, J.G., Santin, C., Kolden, C., Doerr, S.H., Le Quere, C., 2022. Global and regional trends and drivers of fire under climate change. Rev. Geophys. 60.
Justino, F., Bromwich, D.H., Schumacher, V., DaSilva, A., Wang, S.H., 2022. Arctic oscillation and Pacific-north American pattern dominated-modulation of fire danger and wildfire occurrence. Npj Climate Atmos. Sci. 5.
Kang, S.C., Zhang, Y.L., Qian, Y., Wang, H.L., 2020. A review of black carbon in snow and ice and its impact on the cryosphere. Earth Sci. Rev. 210.
Kasischke, E.S., Turetsky, M.R., 2006. Recent changes in the fire regime across the north American boreal region - spatial and temporal patterns of burning across Canada and Alaska. Geophys. Res. Lett. 33.
Kennedy, R.E., Yang, Z., Cohen, W.B., 2010. Detecting trends in forest disturbance and recovery using yearly Landsat time series: 1. LandTrendr - temporal segmentation algorithms. Remote Sens. Environ. 114, 2897–2910.
Key, C.H., Benson, N.C., 2006. Landscape assessment (LA) sampling and analysis methodsd. LA-1-LA-51.
Key, J., Liu, Y., Wang, X., Program, N.C., 2019a. NOAA Climate Data Record (CDR) of AVHRR Polar Pathfinder (APP) Cryosphere, Version 2.0. NOAA National Centers for Environmental Information (NCEI).
Key, J., Wang, X., Liu, Y., Program, N.C., 2019b. NOAA Climate Data Record of AVHRR Polar Pathfinder Extended (APP-X), Version 2 (NOAA National Centers for Environmental Information).
Kharuk, V.I., Ponomarev, E.I., Ivanova, G.A., Dvinskaya, M.L., Coogan, S.C.P., Flannigan, M.D., 2021. Wildfires in the Siberian taiga. Ambio 50, 1953–1974.
Krawchuk, M.A., Moritz, M.A., Parisien, M.A., Van Dorn, J., Hayhoe, K., 2009. Global Pyrogeography: the current and future distribution of wildfire. PLoS One 4.
Krylov, A., McCarty, J.L., Potapov, P., Loboda, T., Tyukavina, A., Turubanova, S., Hansen, M.C., 2014. Remote sensing estimates of stand-replacement fires in Russia, 2002-2011. Environ. Res. Lett. 9.
Kukavskaya, E.A., Buryak, L.V., Shvetsov, E.G., Conard, S.G., Kalenskaya, O.P., 2016. The impact of increasing fire frequency on forest transformations in southern Siberia. For. Ecol. Manag. 382, 225–235.

Kurbanov, E., Vorobev, O., Lezhnin, S., Sha, J.M., Wang, J.L., Li, X.M., Cole, J., Dergunov, D., Wang, Y.B., 2022. Remote sensing of Forest burnt area, burn severity, and post-fire recovery: a review. Remote Sens. 14.
LAADS, N, 2022. MetOp-B-Derived AVHRR Products Available in the Long-Term Data Record Collection. NASA LAADS.
Li, C.C., Li, H.J., Li, J.Z., Lei, Y.P., Li, C.Q., Manevski, K., Shen, Y.J., 2019. Using NDVI percentiles to monitor real-time crop growth. Comput. Electron. Agric. 162, 357–363.
Liu, Y.Q., Stanturf, J., Goodrick, S., 2010. Trends in global wildfire potential in a changing climate. For. Ecol. Manag. 259, 685–697.
Liu, P., Liu, Y., Guo, X., Zhao, W., Wu, H., Xu, W., 2023. Burned area detection and mapping using time series Sentinel-2 multispectral images. Remote Sens. Environ. 296.
Lizundia-Loiola, J., Oton, G., Ramo, R., Chuvieco, E., 2020. A spatio-temporal active-fire clustering approach for global burned area mapping at 250 m from MODIS data. Remote Sens. Environ. 236.
Lizundia-Loiola, J., Franquesa, M., Khairoun, A., Chuvieco, E., 2022. Global burned area mapping from Sentinel-3 synergy and VIIRS active fires. Remote Sens. Environ. 282.
Martin, P., Gomez, I., Chuvieco, E., 2006. Burnt area index (BAIM) for bunred area discrimination at regional scale using MODIS data. For. Ecol. 234, S221.
Mhawej, M., Faour, G., Adijizian-Gerard, J., 2015. Wildfire Likelihood's Elements: A Literature Review, pp. 282–293. Challenges.
Morgan, P., Keane, R., Dillon, G., Jain, T., Hudak, A., Karau, E., Sikkink, P., Holden, Z., Strand, E., 2014. Challenges of assessing fire and burn severity using field measures, remote sensing and modelling. Int. J. Wildland Fire 23, 1045–1060.
Mouillot, F., Schultz, M.G., Yue, C., Cadule, P., Tansey, K., Ciais, P., Chuvieco, E., 2014. Ten years of global burned area products from spaceborne remote sensing-a review: analysis of user needs and recommendations for future developments. Int. J. Appl. Earth Obs. Geoinf. 26, 64–79.
MTBS, M. T. i. B. S, 2022. Burned Areas Boundaries Dataset. US Geological Survey.
NRC, 2024. National Burned Area Composite (NBAC). Canadian Forest Service, Northern Forestry Centre, Edmonton, Alberta: Natural Resources Canada.
Ohata, S., Koike, M., Yoshida, A., Moteki, N., Adachi, K., Oshima, N., Matsui, H., Eppers, O., Bozem, H., Zanatta, M., Herber, A.B., 2021. Arctic black carbon during PAMARCMiP 2018 and previous aircraft experiments in spring. Atmos. Chem. Phys. 21, 15861–15881.
Olofsson, P., Foody, G.M., Herold, M., Stehman, S.V., Woodcock, C.E., Wulder, M.A., 2014. Good practices for estimating area and assessing accuracy of land change. Remote Sens. Environ. 148, 42–57.
Olson, D.M., Dinerstein, E., Wikramanayake, E.D., Burgess, N.D., Powell, G.V.N., Underwood, E.C., D'amico, J.A., Itoua, I., Strand, H.E., Morrison, J.C., Loucks, C.J., Allnutt, T.F., Ricketts, T.H., Kura, Y., Lamoreux, J.F., Wettengel, W.W., Hedao, P., Kassem, K.R., 2001. Terrestrial ecoregions of the world: a new map of life on Earth: a new global map of terrestrial ecoregions provides an innovative tool for conserving biodiversity. BioScience 51, 933–938.
Oton, G., Ramo, R., Lizundia-Loiola, J., Chuvieco, E., 2019. Global detection of long-term (1982-2017) burned area with AVHRR-LTDR data. Remote Sens. 11.
Oton, G., Lizundia-Loiola, J., Pettinari, M.L., Chuvieco, E., 2021. Development of a consistent global long-term burned area product (1982-2018) based on AVHRR-LTDR data. Int. J. Appl. Earth Obs. Geoinf. 103.
Oton, G., Pereira, J.M.C., Silva, J.M.N., Chuvieco, E., 2021b. Analysis of Trends in the FireCCI Global Long Term Burned Area Product (1982-2018). Fire-Switzerland, p. 4.
Pan, Y.D., Birdsey, R.A., Fang, J.Y., Houghton, R., Kauppi, P.E., Kurz, W.A., Phillips, O.L., Shvidenko, A., Lewis, S.L., Canadell, J.G., Ciais, P., Jackson, R.B., Pacala, S.W., McGuire, A.D., Piao, S.L., Rautiainen, A., Sitch, S., Hayes, D., 2011. A large and persistent carbon sink in the world's forests. Science 333, 988–993.
Pasquarella, V., Arévalo, P., Bratley, K., Bullock, E., Gorelick, N., Yang, Z., Kennedy, R., 2022. Demystifying LandTrendr and CCDC temporal segmentation. Int. J. Appl. Earth Obs. Geoinf. 110, 102806.
Pausas, J.G., Keeley, J.E., 2021. Wildfires and global change. Front. Ecol. Environ. 19, 387–395.
Petropoulos, G.P., Vadrevu, K.P., Xanthopoulos, G., Karantounias, G., Scholze, M., 2010. A comparison of spectral angle mapper and artificial neural network classifiers combined with Landsat TM imagery analysis for obtaining burnt area mapping. Sensors 10, 1967–1985.
Phillips, C.A., Rogers, B.M., Elder, M., Cooperdock, S., Moubarak, M., Randerson, J.T., Frumhoff, P.C., 2022. Escalating carbon emissions from north American boreal forest wildfires and the climate mitigation potential of fire management. Sci. Adv. 8.
Pinty, B., Verstraete, M., 1992. GEMI: A Non-linear Index to Monitor Global Vegetation from Satellites. Vegetatio, pp. 15–20.
Pithan, F., Mauritsen, T., 2014. Arctic amplification dominated by temperature feedbacks in contemporary climate models. Nat. Geosci. 7, 181–184.
Ponomarev, E.I., Kharuk, V.I., Ranson, K.J., 2016. Wildfires dynamics in Siberian larch forests. Forests 7.
Pullabhotla, H., Zahid, M., Heft-Neal, S., Rathi, V., Burke, M., 2023. Global biomass fires and infant mortality. Proc. Natl. Acad. Sci. USA 120.
Ratajczak, Z., Carpenter, S.R., Ives, A.R., Kucharik, C.J., Ramiadantsoa, T., Stegner, M.A., Williams, J.W., Zhang, J., Turner, M.G., 2018. Abrupt change in Ecological systems: inference and diagnosis. Trends Ecol. Evol. 33, 513–526.
Reich, P., Bermudez, R., Montgomery, R., Rich, R., Rice, K., Hobbie, S., Stefanski, A., 2022. Even modest climate change may lead to major transitions in boreal forests. NATURE 608, 540-+.
Roger, J.C., Santamaria, A., Ray, J.P., Villaescusa Nadal, J.L., Vermote, E., Devadiga, S., 2023. LTDR AVHRR Products (Version 6) User Guide. National Aeronautics and Space Administration.
Shvidenko, A.Z., Shchepashchenko, D.G., Vaganov, E.A., Sukhinin, A.I., Maksyutov, S.S., McCallum, I., Lakyda, I.P., 2011. Impact of wildfire in Russia between 1998-2010 on ecosystems and the global carbon budget. Dokl. Earth Sci. 441, 1678–1682.
Sobrino, J.A., Julien, Y., 2013. Trend analysis of global MODIS-Terra vegetation indices and land surface temperature between 2000 and 2011. Ieee J. Selected Top. Appl. Earth Observat. Remote Sens. 6, 2139–2145.
Soja, A.J., Shugart, H.H., Sukhinin, A., Conard, S., Stackhouse Jr., P.W., 2006. Satellite-derived mean fire return intervals as indicators of change in Siberia (1995-2002). Mitig. Adapt. Strateg. Glob. Chang. 11, 75–96.
Soja, A.J., Tchebakova, N.M., French, N.H.F., Flannigan, M.D., Shugart, H.H., Stocks, B. J., Sukhinin, A.I., Parfenova, E.I., Chapin, F.S., Stackhouse, P.W., 2007. Climate-induced boreal forest change: predictions versus current observations. Glob. Planet. Chang. 56, 274–296.
Talucci, A.C., Loranty, M.M., Alexander, H.D., 2022. Siberian taiga and tundra fire regimes from 2001-2020. Environ. Res. Lett. 17.
Tian, J.X., Chen, X.N., Cao, Y.F., Chen, F., 2022. Satellite Observational Evidence of Contrasting Changes in Northern Eurasian Wildfires from 2003 to 2020. *Remote Sensing*, p. 14.
Tomshin, O., Solovyev, V., 2021. Spatio-temporal patterns of wildfires in Siberia during 2001–2020. Geocarto Int. 7339–7357.
Veraverbeke, S., Rogers, B.M., Goulden, M.L., Jandt, R.R., Miller, C.E., Wiggins, E.B., Randerson, J.T., 2017. Lightning as a major driver of recent large fire years in north American boreal forests. *Nature*. Climate Change 7, 529.
Verbesselt, J., Hyndman, R., Newnham, G., Culvenor, D., 2010. Detecting trend and seasonal changes in satellite image time series. Remote Sens. Environ. 114, 106–115.
Vermote, E., Justice, C., Csiszar, I., Eidenshink, J., Myneni, R., Baret, F., Masuoka, E., Wolfe, R., 2022. Advanced Very High Resolution Radiometer (AVHRR). Long Term Data Record NASA Goddard Space Flight Center.
Walker, X.J., Baltzer, J.L., Cumming, S.G., Day, N.J., Ebert, C., Goetz, S., Johnstone, J.F., Potter, S., Rogers, B.M., Schuur, E.A.G., Turetsky, M.R., Mack, M.C., 2019. Increasing wildfires threaten historic carbon sink of boreal forest soils. Nature 572, 520–+.
Wang, Z., Ma, Y., Zhang, Y., Shang, J., 2022. Review of remote sensing applications in grassland monitoring. Remote Sens. 14.
Watts, L., Laffan, S., 2014. Effectiveness of the BFAST algorithm for detecting vegetation response patterns in a semi-arid region. In Remote Sens. Environ. 234–245.
White, C.H., Heidinger, A.K., Ackerman, S.A., McIntyre, P.B., 2018. A long-term fine-resolution record of AVHRR surface temperatures for the Laurentian Great Lakes. Remote Sens. 10.
Whitman, E., Parisien, M.A., Thompson, D.K., Flannigan, M.D., 2019. Short-interval wildfire and drought overwhelm boreal forest resilience. Sci. Rep. 9.
Wirth, C., 2005. Fire Regime and Tree Diversity in Boreal Forests: Implications for the Carbon Cycle, pp. 309–344.
Zhu, Z., 2017. Change detection using landsat time series: a review of frequencies, preprocessing, algorithms, and applications. In ISPRS J. Photogrammetry Remote Sens. 370–384.
Zhu, Z., Woodcock, C.E., 2014. Continuous change detection and classification of land cover using all available Landsat data. Remote Sens. Environ. 144, 152–171.
Zhu, Z., Woodcock, C., Olofsson, P., 2012. Continuous monitoring of forest disturbance using all available Landsat imagery. In Remote Sens. Environ. 75–91.